Photophysics of the polymer acceptor PF5-Y5 in organic photovoltaics:

A FIRST-PRINCIPLES THEORY-BASED STUDY

Fotofysik hos polymeracceptorn PF5-Y5 i organiska solceller:
En teoribaserad studie

Anton Almén

Faculty of Health, Science and Technology

Master of Science in Engineering Physics

30 hp (ECTS)

Supervisor: Moyses Araujo & Cleber Marchiori

Examiner: Lars Johansson

Date: 2021-12-24

Abstract

Non-fullerene Acceptors (NFAs) have gathered a great deal of interest for use in organic photovoltaics (OPVs) due to recent breakthroughs in their power conversion efficiency and other advantages they offer over their Fullerene-based counterparts.

In this work, a new promising non-fullerene polymer acceptor, PF5-Y5, have been studied using density functional theory and time-dependent density functional theory; and the effects that oligomer length, geometry relaxation and exchange-correlation interaction has on the exciton binding energies (the difference between optical and fundamental energy gaps) have been investigated.

Both the fundamental and optical gaps are significantly affected by the choice of functional (i.e., the description of the exchange-correlation interaction). However, it does not appear to significantly impact obtained exciton binding energies as the effects of the fundamental and optical gaps cancel each other out.

Both the fundamental and optical energy gap are shown to slightly reduce as a function of the oligomer length ($\sim 0.1 - 0.3\ eV$ reduction for each repeated monomer). As both gaps are reduced by a similar amount per repeated monomer, they counteract each other and the total effect that oligomer length has on the exciton binding energy is very low.

Geometry relaxation and thermal effects showed the largest impact on the fundamental gap and exciton binding energy, with their combined effect resulting in a $\sim 0.5\ eV$ reduction in binding energy.

Sammanfattning

Non-Fullerene Acceptorer (NFAs) har rönt stort intresse för användning i organiska solceller (OPVs) på grund av genombrott på senare tid gällande deras effektomvandlingsverkningsgrad och en mängd andra fördelar som de erbjuder jämfört med sina fullerene-baserade motsvarigheter.

I det här arbetet har en ny lovande polymer-acceptor, PF5-Y5, studerats med hjälp av täthetsfunktionalteori (DFT) och tidsberoende täthetsfunktionsteori (TD-DFT). Effekterna som oligomerlängd, geometri-avslappning och utbytes-korrelations-interaktion har på exciton-bindningsenergin (skillnaden mellan optiska och fundamentala energigapen) har även undersökts.

Både erhållna värden för det fundamentala och optiska gapet påverkas avsevärt av valet av funktional (dvs. beskrivningen av utbytes-korrelations-interaktionen). Valet av funktional verkar dock inte nämnvärt påverka erhållna värden för exciton-bindningsenergin då effekterna från det fundamentala och optiska gapen till stor del tar ut varandra.

Både det fundamentala och optiska energigapet minskar som en funktion av oligomerlängden ($\sim 0.1 - 0.3\ eV$ minskning för varje upprepad monomer). Eftersom båda energigapen minskar ungefär lika mycket för varje upprepad monomer så motverkar de till stor grad varandra; och den totala effekten som oligomerlängd har på exciton-bindningsenergin förblir låg.

Strukturell relaxation (eng: geometry relaxation) och termiska effekter visade sig ha störst påverkan på det fundamentala energigapet och exciton-bindningsenergin, och deras sammanlagda effekt ledde till en $\sim 0{,}5\ eV$ reduktion i bindningsenergi.

Acknowledgements

First, I would like to thank my supervisors Moyses Araujo & Cleber Marchiori for our many discussions and for all their insights into this subject they have bestowed upon me. I must also thank Leandro Franco for our discussions and for his many helpful insights, and helping me solve problems I have encountered, particularly regarding the solvation model, absorption spectrum calculations and testing for potential spin contamination.

Finally, I would like to thank my family and close friends for their support throughout these years, and for making every day a good day.

Anton Almén

Contents

1 Introduction

Non-Fullerene Acceptors (NFAs) are receiving a great deal of attention due to recent breakthroughs in the power conversion efficiency of organic photovoltaic devices obtained with this type of materials [1]. However, a fundamental understanding of the underlying photophysics of the NFAs and related polymers is still lacking. NFAs are able of absorbing light in the visible range opening a new channel for charge photogeneration, which involves a hole-transfer process from the acceptor to the donor. Here, many fundamental questions arise, including: (i) the exciton-state energy transfer at the interfaces; (ii) the low non-radiative voltage losses and high photocurrent generation and external quantum efficiency in low-gap systems and (iii) exciton dissociation at interfaces with low ionization potential and electron affinity offsets. To shed light on these technologically relevant problems, a fundamental understanding of the underlying photophysics of each component is needed. In this study, an atomic-scale modelling of the recently proposed polymer-acceptor [2], PF5-Y5, has been carried out within the framework of density functional theory (DFT) and time-dependent-DFT (TDDFT). The fundamental electrochemical gap (difference between the redox potentials) has been calculated from the full Gibbs free energies and compared with commonly used approximations such as the *vertical transition* approach. This methodology will allow an assessment of the relevance of the redox-processes' thermodynamics on the exciton binding energies (the difference between optical and fundamental gaps). These properties have been shown to play an important role for the efficient hole-transfer processes [3] [4]. The electronic transitions and optical spectra have been calculated using TDDFT. The effect of the oligomer length, geometry relaxation and exchange-correlation interaction has also been investigated. It is expected that such fundamental study will provide guidelines to the development of novel molecular NFAs; providing a steppingstone for NFA based organic photovoltaics to reach the efficiency threshold where organic photovoltaics can be considered commercially viable alternatives to silicon-based devices. A goal which is not only technologically relevant, but also comes with environmental and economic benefits owning to the fact that organic photovoltaics have much wider potential for device-integration than silicon-based cells, leading to more potential markets as well as a larger

total energy generation coming from photovoltaics compared to less environmentally friendly alternatives such as coal or oil.

1.1 Thesis layout

The layout of this paper is as follows. Sections (2) and (3) presents both a brief history and accompanying theory of organic photovoltaics and computational quantum physics respectively, with an emphasis on the main materials and methods used. In section (4), the experimental procedure and methods for data acquisition is described. The result of this thesis is given in section (5) along with a discussion of the obtained results. Section (6) and (7) closes out this thesis with a conclusion and brief outlook.

2 Organic photovoltaics

Organic photovoltaics (OPVs) have gathered a lot of interest in the last couple of decades due to their potential as a low-cost alternative to conventional silicon-based solar cells. OPVs, as the name suggests, are made from organic material, and is not a single technology, but rather a group of emerging PV technologies offering multiple advantages over their inorganic counterparts. These advantages include but are not limited to the following:

- Made from cheap and abundant materials (main chemical element is carbon).
- Processable on a large-scale (e.g., by roll-to-roll printing) [5].
- Flexible and lightweight, yet mechanically stable (particularly in the case of all-polymer OPVs) [2].
- Chemical tailoring of molecular properties (e.g., by functionalizing molecular end groups).

The peak efficiencies achieved in OPVs, as well as their operational stability and expected lifetime is still lacking compared to inorganic cells [6]. However, OPVs are a much younger technology and have in recent years seen rapid improvements, particularly in cell efficiency, as illustrated in Figure 2.1.

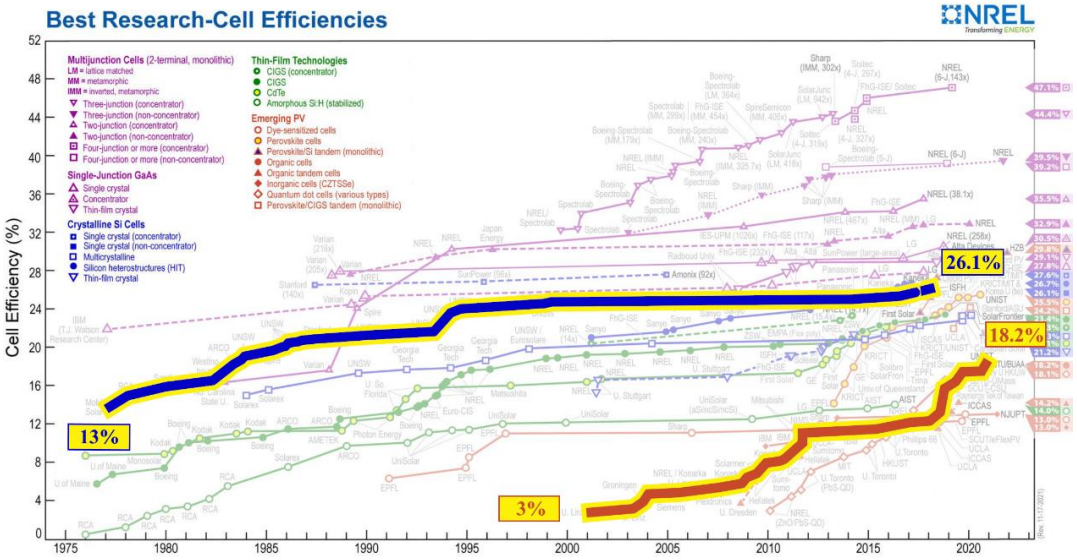

Figure 2.1. NREL's solar cell efficiency chart. The marked blue line shows single crystal silicon solar cells and the orange/brown line show organic solar cells. Adapted from [7].

2.1 Device characterization: Terminology

> *The energy gap between the highest occupied and lowest unoccupied electronic levels is a critical parameter determining the electronic, optical, redox, and transport (electrical) properties of a material. However, the energy gap comes in many flavors, such as the band gap, HOMO–LUMO gap, fundamental gap, optical gap, or transport gap, with each of these terms carrying a specific meaning. Failure to appreciate the distinctions among these different energy gaps has caused much confusion in the literature, which is manifested by the frequent use of improper terminology, in particular, in the case of organic molecular or macromolecular materials.*
>
> *– Jean-Luc Bredas*

In this subchapter, which is heavily based on Jean-Luc Bredas excellent article, *Mind the gap!* [8], the specifics of above-mentioned gaps and a few other important terms relevant for OPV characterization will be presented.

HOMO-LUMO gap: Defined as the energy difference between the (highest occupied molecular orbit) HOMO and (lowest unoccupied molecular orbit) LUMO of a molecule. Experimentally measured as the energy difference between the ground state molecule (N electrons) and ionized state molecules ($N \pm 1$ electrons) for HOMO and LUMO levels respectively. Computationally, this is calculated on the neutral ground state molecule (N electrons) by diagonalizing the Schrodinger equation (or Kohn-Sham equation in the case of DFT). In accordance with Koopman's theorem, one specifically considers the HOMO level to be minus the vertical ionization potential (IP), and the LUMO level to be minus the vertical electron affinity (EA).

Since the computational and experimental approach for obtaining the HOMO-LUMO gap do not consider precisely the same states (the computational approach only considers the ground state while the experimental approach considers both ground state and ionized states), one should be careful with computationally obtained HOMO-LUMO gaps and only consider it an approximation to the fundamental gap.

The fundamental gap: Defined as the difference between a molecule's vertical electron affinity and vertical ionization potential

$$E_{fund} = EA - IP. \tag{2.1}$$

Computationally the electron affinity and ionization potential are calculated from the total energy of the ground state for the neutral molecule (N electrons) and the ground state ions ($N \pm 1$ electrons). More precisely, the electron affinity and ionization potentials are calculated as follows:

$$EA = E_{GS}^{-}(N+1) - E_{GS}^{0}(N) \tag{2.2}$$

$$IP = E_{GS}^{0}(N) - E_{GS}^{+}(N-1) \tag{2.3}$$

where the subscript GS indicates that the molecule is in its ground state, the superscript indicating the total charge of the molecule and the values in parenthesis indicate the total number of electrons. Thermodynamically, EA and IP can also be derived from the half-cell redox potentials $\Phi_{Red/Ox}$, which are usually given in terms of the difference in Gibbs free energy ΔG for a molecule in solution, transitioning between neutral ground state (N electrons) and ionic state ($N \pm 1$ electrons):

$$EA = \Phi_{Red} = -\frac{\Delta G_{(solv)}(Red)}{nF} = -\frac{\mathrm{G}^{-}(N+1) - G^{0}(N)}{nF}, \tag{2.4}$$

$$\mathrm{IP} = \Phi_{Ox} = -\frac{\Delta G_{(solv)}(Red)}{nF} = -\frac{\mathrm{G}^{0}(N) - G^{+}(N-1)}{nF}. \tag{2.5}$$

Here F is the Faraday constant ($= 96485.341\ \mathrm{C/mol}$) and n is the number of electrons involved (which in this case is simply one). An expression for the fundamental gap, written in terms of the redox potentials, is obtained by inserting (2.4) and (2.5) into (2.1), yielding:

$$E_{fund} = \Phi_{Red} - \Phi_{Ox}. \tag{2.6}$$

Since the fundamental gap is computationally obtained from the energy of the neutral molecule (N electron) and charged ions ($N \pm 1$ electron), i.e., the same states one deals with experimentally, it compares closer to experimental values than what computed HOMO-LUMO gaps do.

Optical gap: Defined as the energy of the lowest accessible transition via photon absorption, i.e., the energy difference between the ground state (S_0) and first excited state (S_1) of a molecule. Computationally obtained from time-dependent transition state calculations on the neutral molecule (N electrons). Experimentally the optical gap can be obtained from ultraviolet-visible (UV-vis) spectroscopy.

In organic materials, the optical gap can be substantially lower than the fundamental gap due to the strong exciton (bound electron-hole pair) binding energies commonly present in such materials.

Exciton binding energy (E_b): A measurement of how strongly an exciton is bound by the Coulomb interaction between its electron and hole. The exciton binding energy is defined as the difference between a materials fundamental and optical gap [4]:

$$E_b = E_{fund} - E_{opt}. \tag{2.7}$$

A visual representation of how the exciton binding energy, fundamental gap, optical gap, ionization potential and electron affinity relate to one another can been seen in Figure 2.2.

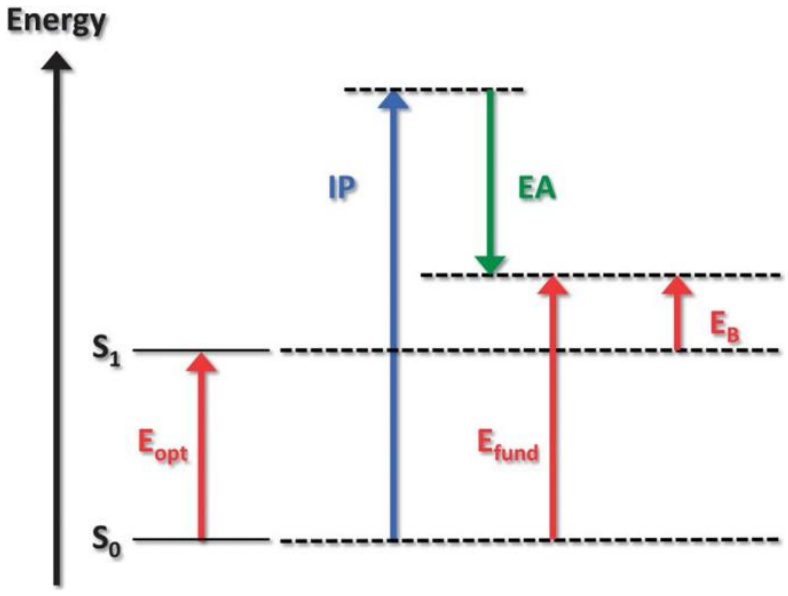

Figure 2.2. Energy level diagram depicting how the optical gap E_{opt} and fundamental gap E_{fund} are defined and how they combine to form the exciton binding energy E_b. [8]

Bandgap (or transport gap): Defined as the energy difference between the top of the valence band and bottom of the conduction band. Can be thought of as the material equivalent to the molecular fundamental gap. Can therefore also be defined as the difference between IP and EA.

Power conversion efficiency (PCE): Defined as the ratio between maximum electrical power output ($= max(J \times V)$) and the power input, i.e., power of the incoming light ($= P_{in}$).

$$PCE = \frac{max(J \times V)}{P_{in}} = FF\frac{J_{SC} \times V_{oc}}{P_{in}}. \quad (2.8)$$

Here, V_{oc} is the open-circuit voltage, J_{sc} is the short-circuit current and FF is the fill factor which is defined as follows:

$$FF = \frac{max(J \times V)}{J_{SC} \times V_{oc}}. \quad (2.9)$$

One of the most important parameters for OPV device characterization.

External quantum efficiency (EQE): Defined as the ratio between the number of charges extracted from the OPV (N_e) and the number of incident photons of a particular wavelength (N_i):

$$EQE = \frac{N_e}{N_i}. \quad (2.10)$$

The EQE is used to characterize how efficient an OPV generates current at specific wavelengths of light and gives information about which use cases (ranges of wavelength) a particular OPV will be most efficient.

2.2 Absorption spectra and the Franck-Condon principle

To properly understand the absorption spectra of a polymer (or rather, of an oligomer) donor or acceptor material, we must first understand a few key ideas:

(i) In quantum mechanics, the energy of a photon can be expressed in terms of the wavelength:

$$E = \frac{hc}{\lambda}, \quad (2.11)$$

where h is Planck's constant ($= 6.62607015 \times 10^{-34}\, m^2 kg s^{-1}$), c is the speed of light and λ is the photon's wavelength.

(ii) Molecular orbits can be expressed as a linear combination of atomic orbitals and depending on if the overlap is constructive or destructive, either bonding or anti-bonding (*) orbitals are formed. Bonding orbitals decrease the energy while anti-bonding orbitals increase the energy. As such, bonding-orbitals are filled with electrons before their anti-bonding counterparts, which is illustrated in Figure 2.3. Overlapping s-orbitals will form σ-orbitals and overlapping p-orbitals will form π-orbitals.

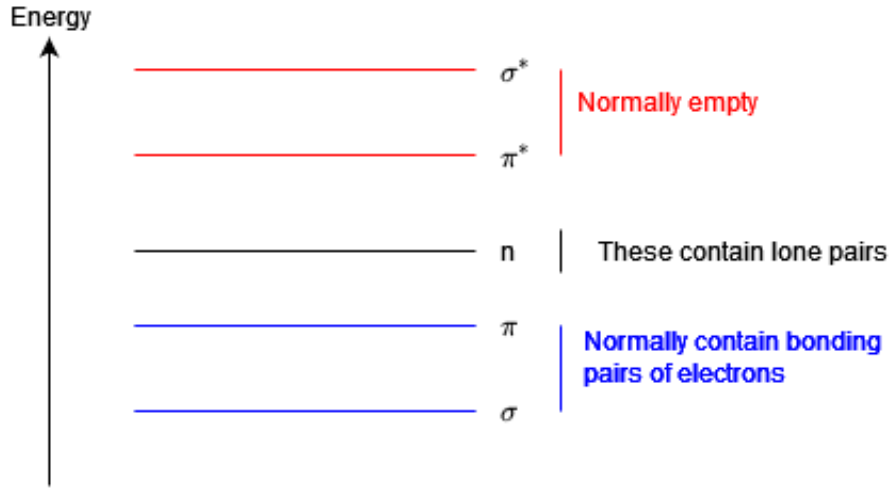

Figure 2.3. Schematic view of the relative energy of molecular orbits. σ and π are bonding orbitals, n is a non-bonding orbital, σ^* and π^* are anti-bonding orbitals. Adapted from [9].

(iii) If a photon passing through a molecule has an energy that matches the energy difference between an orbital containing an electron and an empty orbital, the photon can be absorbed by the electron, promoting it from the lower to the higher energy level.

(iv) The total amount of energy levels in an oligomer increases as the chain length of the oligomer increases. Simultaneously, the bandgap of the oligomer will decrease, as illustrated in Figure 2.4. The absorption onset (largest wavelength associated with an electronic transition) is tied to the first electronic transition, and therefore also the optical gap (since photon energy is inversely proportional to wavelength, as stated in (2.11)). As such, when the oligomer length goes up, the optical gap decreases and the absorption onset becomes redshifted, meaning that it shifts toward longer wavelengths.

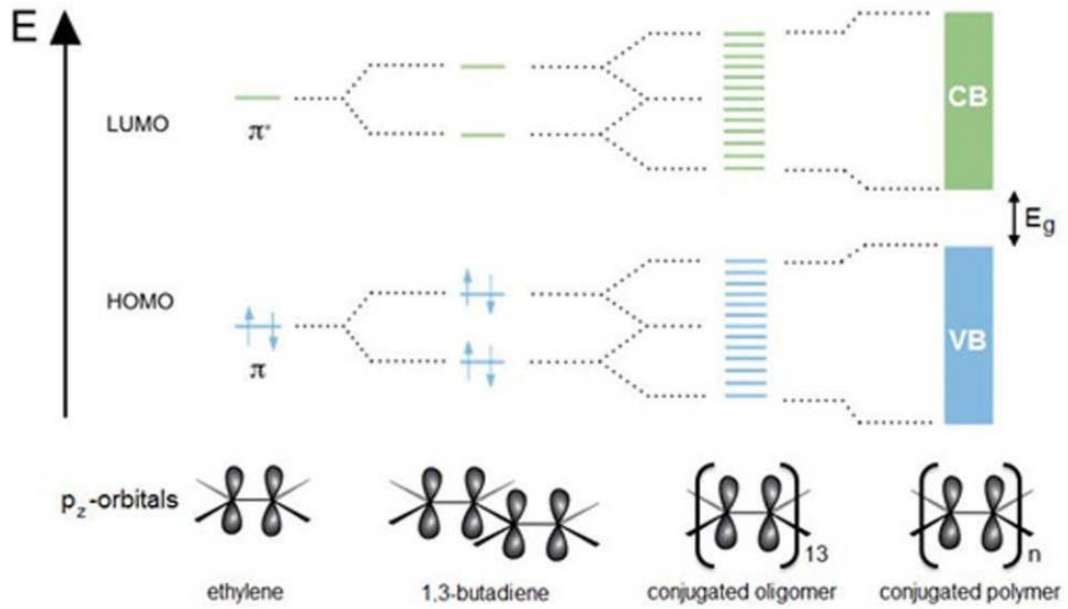

Figure 2.4. Schematics of how the energy levels and bandgap E_g changes as the oligomer length increases. [10]

(v) When an electron is excited from its ground state to a higher energy state, the equilibrium position of the atoms in a molecule will shift slightly. The motion of electrons is much faster than that of the nucleons (protons and neutrons). Therefore, when an electron is excited, the transition happens much faster than the time it takes for the nuclei of the molecule to relax into their new equilibrium positions. As such, electronic transitions can be approximated to occur without any appreciable change in the position of the nuclei. This is called the Franck-Condon principle and is illustrated in Figure 2.5.

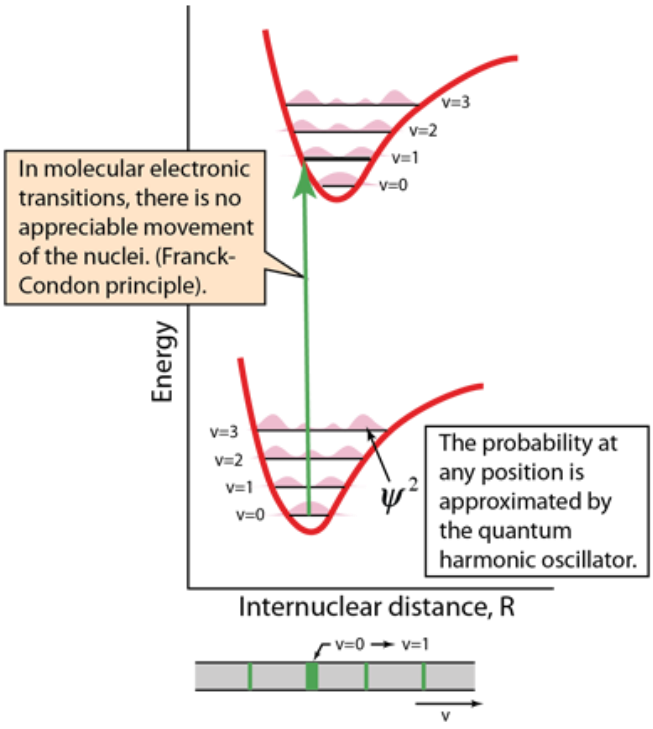

Figure 2.5. Energy diagram depicting the Franck-Condon principle. The curve at the bottom represents the electronic ground state and the curve at the top represents the electronic excited state [11].

If we were to generate an absorption spectrum from the above stated ideas, each transition would be infinitely thin (as the incoming photon energy, and therefore also its wavelength, must exactly match the difference between two energy levels in the molecule). However, this type of spectrum (called a stick spectrum) does not account for the finite lifetime of excited states.

Assuming that the energy and lifetime of an excited state is tied to the uncertainty in energy and uncertainty in time, as expressed in Heisenberg's uncertainty relation:

$$\Delta E \Delta t \geq \hbar \tag{2.12}$$

we find that because an excited state does not have an infinite lifetime, neither should the excitation energy be perfectly well defined. As such, the absorption peaks will broaden, with maximum intensity located at the vertical transition energies. Two other types of broadening also occur, called pressure (or collision) broadening, and doppler broadening. The detailed mechanics of these types of broadening will be left out, but one important property for all three types of broadening is the overall effect, or shape, they cause. Both lifetime and pressure broadening has a Lorentzian distribution shape

to their effect, while the effects of doppler broadening has the shape of a Gaussian distribution [12]. More realistic absorption spectra can thus be achieved by dressing a stick spectrum with either a convolution of Lorentzian, Gaussian, or Voigt (combination of Lorentzian and Gaussian) line shapes centred at the vertical transitions. This method is illustrated in Figure 2.6, in which two computed stick spectra of a hexaazatrinaphthylene (HATN) molecule have been dressed in a convolution of Gaussian line shapes to approximate the absorption spectra of the molecule.

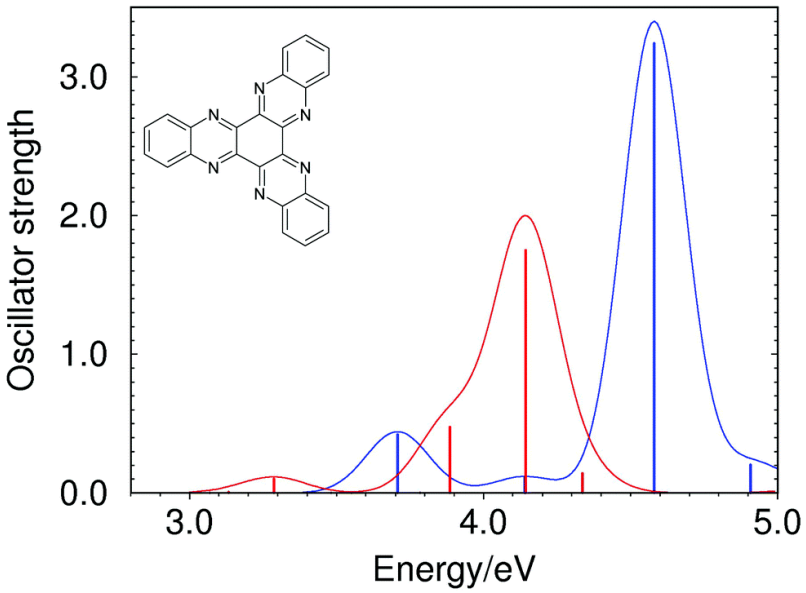

Figure 2.6. Absorption spectrum of HATN (molecule depicted in the top left) computed using two different methods. Here "Oscillator strength" is equivalent to intensity/probability of absorption. The stick spectra (vertical lines) have been dressed in a convolution of Gaussian line shapes (bandwidth = 0.25 eV) [13].

The importance of absorption spectra for OPV characterization is twofold. Firstly, an absorption spectrum gives a visual representation of which wavelengths of incident light the materials can absorb, and how probable the absorption of those specific wavelengths is. Secondly, the absorption onset is tied to the optical gap. By identifying the absorption onset (or in the case of simulations: identify the energy of the first allowed electronic transition) one can determine the optical gap of a donor or acceptor using (2.10).

2.3 Operational basics

OPVs consist of an electron donor, and an electron acceptor material, both consisting of organic materials such as conductive polymers and semiconducting compounds made of small organic molecules. These materials are to a large extent made from chains of carbon atoms and can be considered as large conjugated systems, meaning

that they have chains of alternating single- and double-bonds causing the p-orbitals of neighbouring carbon atoms to overlap. This allows π-electrons to delocalize across the entire conjugated chain (meaning that the electrons are not bound to a single atom, but rather shared between a group of atoms, enabling efficient charge transfer). Figure 2.7 illustrates how overlapping p-orbitals in Benzene, the textbook example of a conjugate system, results in a delocalized π-system.

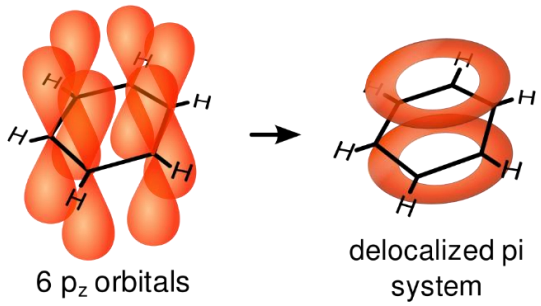

Figure 2.7. Illustration of how the p-orbitals in a benzene ring forms a delocalized π-system. Adapted from [14]

The donor and acceptor materials in OPV devices have their energy levels shifted from one another such that the energy of the highest occupied molecular orbit (HOMO) of the donor is above the HOMO of the acceptor; and similarly, the lowest unoccupied molecular orbit (LUMO) of the donor is above the LUMO of the acceptor, see Figure 2.8.

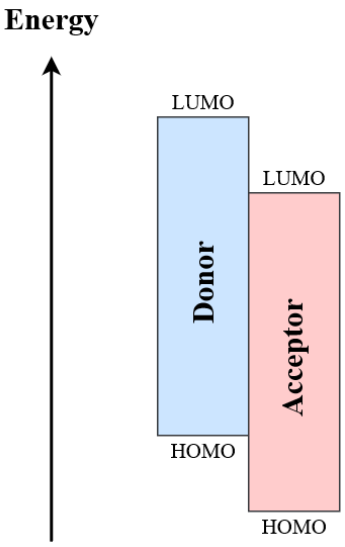

Figure 2.8. Energy diagram showing the alignment of HOMO and LUMO levels in acceptor and donor materials.

Organic semiconductor materials generally have much lower dielectric constants ($\epsilon \approx 2-4$) compared to inorganic semiconductor materials (e.g., silicon: $\epsilon = 12$ and germanium $\epsilon = 16$). As such, the Coulomb interaction holding excitons together is generally much stronger in OPVs, resulting in strongly bound Frenkel excitons that can be localised on a single molecule [15]. As a comparison, loosely bound Wannier-Mott excitons in inorganic PVs can be localized across several lattice parameters.

The operational basics of an OPV device is as a result slightly more complicated compared to an inorganic PV device because additional driving force is required to dissociate the excitons. Furthermore, depending on if an exciton is formed on the acceptor or donor, two different channels for charge photogeneration are possible.

Channel one, also called photoinduced electron transfer (PET), illustrated in Figure 2.9 and Figure 2.10, can be summarized in six steps. (i) A photon with energy equal to the bandgap of the donor material is absorbed inside the donor material, exciting an electron from HOMO to LUMO, leaving behind a positively charged hole at the HOMO (i.e., an exciton is formed in the donor). (ii) The exciton diffuses inside the donor, reaching the interface between acceptor and donor material. (iii) The lower energy level and high electronegativity of the acceptor material causes the electron to jump from donor to acceptor while the hole remains on the donor, forming a charge transfer (CT) state where the electron and hole of the exciton are loosely bound. (iv) The electron and hole are completely dissociated (creating a free electron and hole) due to thermal energy and internal electric fields and disorder caused by the acceptor and donor materials. (v) The now free charges (electron and hole) are transported to the anode and cathode. (vi) The free charges are extracted at the anode (hole) and cathode (electron) respectively.

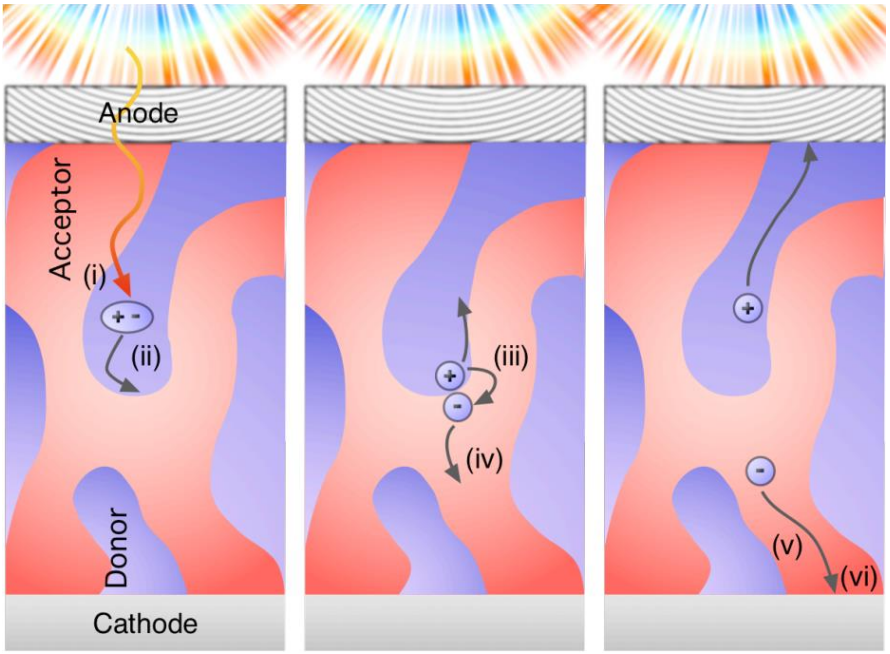

Figure 2.9. Working principle of PET in an OPV device laid out from light absorption to photocurrent generation from a kinematic perspective [16]: (i) Exciton generation, (ii) exciton diffusion, (iii) exciton dissociation, (iv) charge separation, (v) charge carrier transport and (vi) Charge extraction.

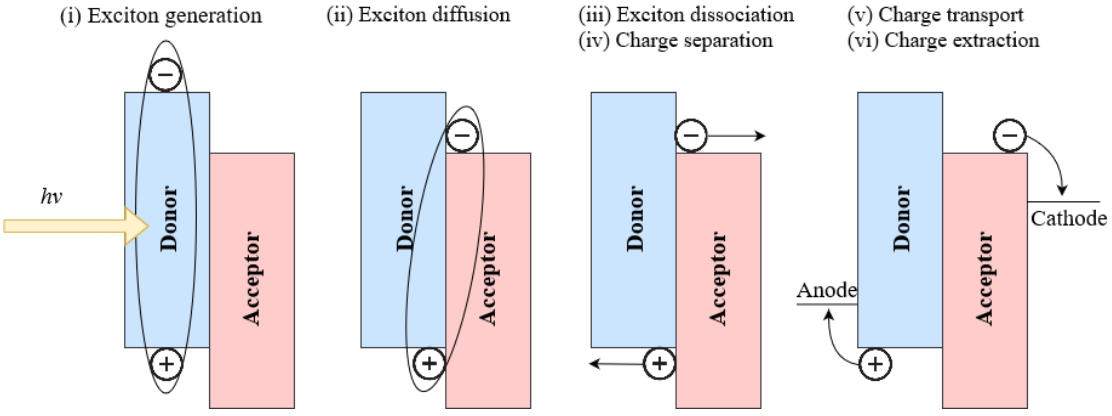

Figure 2.10. Working principle of PET in an OPV device laid out from light absorption to photocurrent generation from a simplified energy diagram perspective.

The second channel, called photoinduced hole transfer (PHT), have a similar working principle, but instead of exciton formation in the donor leading to an electron traveling to the acceptor, the reverse happens; an exciton is formed on the acceptor material leading to a hole travelling to the donor.

The driving force for PET (ΔH_e) and PHT (ΔH_h) can be approximated as the difference in electron affinity (EA) and ionization potential (IP) between the donor and acceptor materials [4].

$$\Delta H_e = EA_D - EA_A \quad (2.13)$$

$$\Delta H_h = IP_A - IP_D \quad (2.14)$$

A sufficient driving force is required to be able to separate the electron and hole once a CT state has formed. However, high driving forces can cause increased voltage losses, limiting the maximum achievable PCE [17].

During charge carrier transport, charges move by hopping between localized states, and free electrons and holes can during this process recombine (either through radiative or nonradiative means) [5]. It is therefore important to have control over the morphology of an OPV device, not only for achieving short distances between donor/acceptor interface, but also to minimize regions where electrons and holes can get trapped and/or recombine.

2.4 Device architecture

To make an OPV device, a minimum of six parts are needed. Two electrodes (anode and cathode), an electron donor material, an electron acceptor material, as well as a hole transport layer (HTL) and an electron transport layer (ETL) coating the respective electrodes. The transport layers serve two purposes:

- To enhance the carrier transport (compared to that of the donor/acceptor materials), quickly moving recently formed electrons/holes away from the donor/acceptor interface, reducing recombination.
- To restrict the flow of electrons/holes to the wrong electrode, minimizing potential leak currents.

The electron donor and acceptor materials are sandwiched between the electrodes, and devices typically fall under one of two architectures, called bilayer heterojunction and bulk heterojunction (BHJ), illustrated in Figure 2.11.

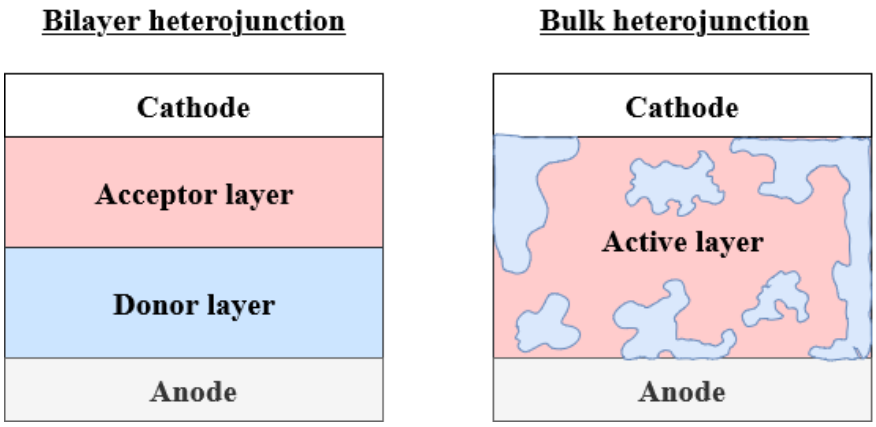

Figure 2.11. OPV device architecture (HTL and ETL omitted for clarity). The left image shows a bilayer heterojunction structure. The right image shows a bulk heterojunction structure.

The bilayer structure separates the acceptor and donor materials into two distinct layers while the bulk heterojunction consists of an intermixed network of both acceptor and donor material in what is called the active layer.

Advantages of the bilayer structure is its well-defined layer geometry and straightforward fabrication process by sequential layer deposition. The first fully functioning OPV device, fabricated in 1986, was based on this design and reached a PCE of roughly 1% [18]. The main drawback of this design is that for optimal light absorption, the layer thickness should be on the same order as the absorption length (roughly 100 nm). However, typical exciton diffusion lengths in organic molecules are much smaller (on the order of 10 nm), limiting the maximum PCE that can be obtained.

The BHJ design solves this problem by intermixing the donor and acceptor materials throughout the entire active layer, allowing for more efficient exciton dissociation as the average distance between donor and acceptor interface is reduced (and the total surface of the donor/acceptor interface is increased). This concept was proven in 1995 by G. Yu et al. who fabricated OPV devices with an active layer consisting of a network made from a semiconductive polymer and a Buckminsterfullerene (C_{60}) derivative, obtaining a PCE of around 2.9% [19].

2.5 Material considerations

As we have seen, the active layer in OPVs consists of two parts, an electron donor, and an electron acceptor. Over the last three decades a significant amount of research have

gone into the development of high efficiency donors; meanwhile only a small amount of acceptors have been successfully used until very recently [5].

We can place OPVs into three major classes: dye-sensitized OPVs (also called Grätzel cells), small-molecule OPVs and polymer based OPVs. Here, common group of materials that are used at large as donor and acceptors for each class are presented.

Dye-sensitized OPVs

- **Acceptor:** Metal oxide compounds such as TiO_2 and ZnO.
- **Donor:** Organic small-molecule dyes.

Small-molecule OPVs

- **Acceptor:** Fullerenes (e.g., C_{60}), organic dyes (e.g., Perylene dyes), and more recently also non-fullerene acceptors (NFAs).
- **Donor:** Highly conjugated small organic molecules.

Polymer OPVs

- **Acceptor:** Fullerene derivatives such as $PC_{60}BM$ or $PC_{70}BM$, and more recently also NFAs.
- **Donor:** Organic polymers.

Excluding Grätzel-cells (which have a significantly different structure compared to other OPV cells) we see that the acceptor materials have been mainly dominated by fullerenes and their derivative.

NFA based OPVs offer considerable improvements in mechanical, thermal, and morphological stability compared to Fullerene Acceptor (FA) based OPVs, and are an ideal fit for cheap large-scale production methods such as roll to roll printing [1]. Historically, the PCE of NFA based OPVs have been substantially lower compared to FA based OPVs due to only achieving either a high V_{oc} or J_{sc}, but not both simultaneously. Recently however, several NFA based devices have overcome this problem and are now offering competitive PCEs compared to their FA based counterparts.

2.5.1 PF5-Y5

PF5-Y5 (the main material investigated in this study), illustrated in Figure 2.12, is a low-bandgap polymer acceptor which was developed in 2020 by coupling the electron-deficient Y5 molecule and the electron donor unit thienyl-benzodithiophen (BDT-T). Alongside the synthesis of PF5-Y5, an accompanying all polymer OPV device (complete device architecture: ITO/PEDOT:PSS/PBDB-T:PF5-Y5/PDINO/Al) was developed which achieved an impressive PCE of 14.45%, which is near the top of its class in performance [2].

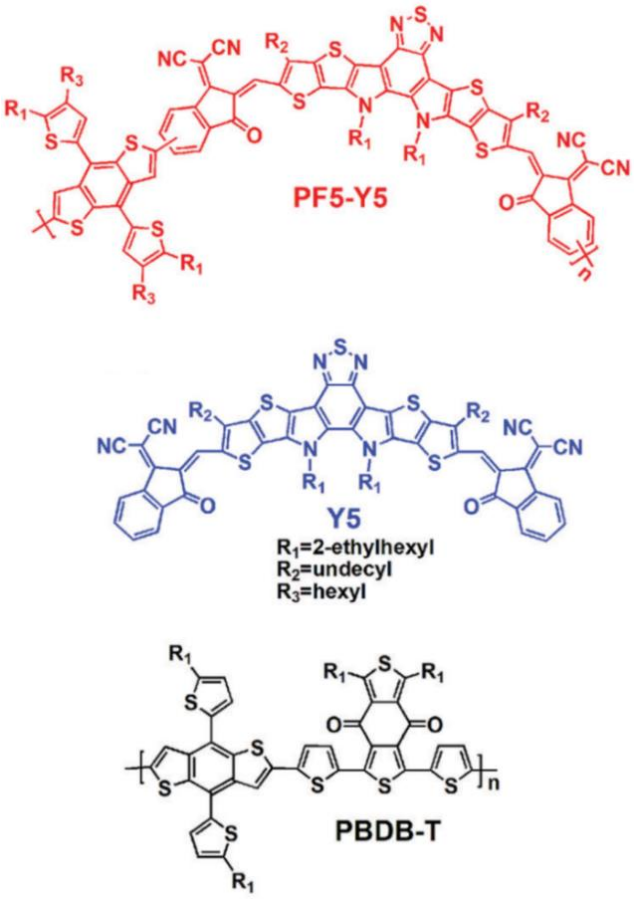

Figure 2.12. Chemical structure of PF5-Y5, Y5 and PBDB-T (the acceptor and donor materials used in the PF5-Y5 based all-polymer OPV device discussed above). Adapted from [2].

PF5-Y5 shows remarkable photoelectric properties with high electron mobility ($3.18 \times 10^{-3}\ cm^2V^{-1}s^{-1}$), absorption onset extending to ~880 nm in thin films and ~850 nm in chlorobenzene solution, high absorption coefficient (~$1.43 \times 10^5\ cm^{-1}$), and a low bandgap ($1.68\ eV$ in neat films) accompanied by a high LUMO energy ($-3.84\ eV$) [2].

3 Computational quantum physics

The holy grail in computational quantum physics is to exactly predict the properties of matter. The electronic structure of atoms, molecules and solids is governed by quantum mechanics, and thus, to exactly predict the electronic structure, an exact solution to the many-body Schrödinger equation

$$\hat{H}\Psi(\boldsymbol{r}_1, \boldsymbol{r}_2, \dots, \boldsymbol{r}_N) = E\Psi(\boldsymbol{r}_1, \boldsymbol{r}_2, \dots, \boldsymbol{r}_N), \tag{3.1}$$

where $\hat{H}$ is the system's Hamiltonian, Ψ is the many-body-wavefunction and E is the total energy of the system, is required. Breaking down atoms into their constituents, electrons and nuclei and account for their Coulomb interaction yields the following Hamiltonian (if one neglects relativistic effects) [20]

$$\begin{aligned}\hat{H} = &-\sum_{i=1}^{M}\frac{\hbar^2}{2m_{Z_i}}\nabla^2_{\boldsymbol{R}_i} - \sum_{i=1}^{N}\frac{\hbar^2}{2m_e}\nabla^2_{\boldsymbol{r}_i} + \frac{1}{4\pi\epsilon_0}\sum_{i=1}^{M}\sum_{j>i}^{M}\frac{Z_i Z_j}{|\boldsymbol{R}_i - \boldsymbol{R}_j|} \\ &-\frac{1}{4\pi\epsilon_0}\sum_{i=1}^{M}\sum_{j=1}^{M}\frac{Z_j e}{|\boldsymbol{r}_i - \boldsymbol{R}_j|} + +\frac{1}{4\pi\epsilon_0}\sum_{i=1}^{N}\sum_{j>i}^{N}\frac{e^2}{|\boldsymbol{r}_i - \boldsymbol{r}_j|},\end{aligned} \tag{3.2}$$

where N and M are the total number of electrons and nuclei of the system, m_e, m_Z, e, Z, $\boldsymbol{r}$ and $\boldsymbol{R}$ are the mass, charge and position of the electrons and nuclei respectively. Solving the many-body Schrödinger equation analytically using this Hamiltonian for anything larger than a handful of electrons and nuclei is not realistically doable, even for very powerful computers [21].

One way to try and circumvent this problem is to apply a set of approximations to simplify the Hamiltonian into a more manageable form. A common approximation is the Born-Oppenheimer approximation, where one assumes the motion of the nuclei and electrons to be independent of each other, and their degrees of freedom to be de-coupled [22]. The Born-Oppenheimer approximation can be justified by considering that the mass of the nuclei is more than 1800 times heavier than the electron, and as such, move at much slower speeds, appearing essentially stationary in the reference frame of moving electrons. Applying the Born-Oppenheimer approximation simplifies the Hamiltonian in (3.2) a great deal, resulting in

$$\widehat{H} = -\sum_{i=1}^{N} \frac{\hbar^2}{2m_e} \nabla_{\boldsymbol{r}_i}^2 + \frac{1}{4\pi\epsilon_0} \sum_{i=1}^{N} \sum_{j=i}^{M} \frac{Z_j e}{|\boldsymbol{r}_i - \boldsymbol{R}_j|} + \frac{1}{4\pi\epsilon_0} \sum_{i=1}^{N} \sum_{j>i}^{N} \frac{e^2}{|\boldsymbol{r}_i - \boldsymbol{r}_j|}. \quad (3.3)$$

Inserting this Hamiltonian into the many-body Schrödinger equation still proves essentially unsolvable for realistic systems such as solid-state materials ($N \gg 10^{10}$) because of the $3N$ coupled degrees of freedom of the many-body wavefunction, Ψ.

Computational methods such as Hartree-Fock (HF), and density functional theory (DFT) have been developed to solve this problem, allowing for practical application.

3.1 The Hartree-Fock method

Hartree initially tried to arrive at a realistically solvable wave equation by approximating electrons as independent particles, ignoring the Pauli exclusion principle. The resulting many-body wavefunction

$$\Psi_{\mathrm{H}}(\boldsymbol{r}_1, \boldsymbol{r}_2, \dots, \boldsymbol{r}_N) = \prod_{i=1}^{N} \psi_i(\boldsymbol{r}_i) \quad (3.4)$$

still have $3N$ degrees of freedom, but since the particles are independent, the degrees of freedom are decoupled from each other. These individual electron wavefunctions are often also called orbitals. Fock [23] and Slater [24], later improved upon Hartree's work by anti-symmetrizing the Hartree wavefunction, resulting in a wavefunction nicely written in the form of a Slater determinant:

$$\begin{aligned} \Psi_{\mathrm{HF}}(\boldsymbol{r}_1, \boldsymbol{r}_2, \dots, \boldsymbol{r}_N) &= S\left[\prod_{i=1}^{N} \psi_i(\boldsymbol{r}_i)\right] \\ &= \frac{1}{\sqrt{N!}} \begin{vmatrix} \psi_1(\boldsymbol{r}_1) & \cdots & \psi_1(\boldsymbol{r}_N) \\ \vdots & \ddots & \vdots \\ \psi_N(\boldsymbol{r}_1) & \cdots & \psi_N(\boldsymbol{r}_N) \end{vmatrix}, \end{aligned} \quad (3.5)$$

which correctly incorporates the effects of electron exchange by abiding to the Pauli exclusion principle.

Using the many-body wavefunction in its Slater determinant form then allows the calculation of a systems total energy according to

$$E_{HF} = \langle \Psi_{HF} | \widehat{H} | \Psi_{HF} \rangle, \quad (3.6)$$

which takes the form [25]

$$E_{HF} = \sum_{i=1}^{N} \left\langle \psi_i \middle| -\frac{\hbar^2 \nabla_{\boldsymbol{r}}^2}{2m_e} + V_{ext} \middle| \psi_i \right\rangle + \frac{e^2}{2} \sum_{i \neq j} \left\langle \psi_i \psi_j \middle| \frac{1}{|\boldsymbol{r} - \boldsymbol{r}'|} \middle| \psi_i \psi_j \right\rangle - \frac{e^2}{2} \sum_{i \neq j} \left\langle \psi_i \psi_j \middle| \frac{1}{|\boldsymbol{r} - \boldsymbol{r}'|} \middle| \psi_j \psi_i \right\rangle, \quad (3.7)$$

where V_{ext} is the Coulomb potential from the nuclei.

The single particle Hartree-Fock equation

$$F\psi_i = \epsilon_i \psi_i \quad (3.8)$$

(HF-framework equivalent to the Schrödinger equation) is then found by minimizing E_{HF} with respect to the orbitals, resulting in

$$\left[-\frac{\hbar^2 \nabla_{\boldsymbol{r}}^2}{2m_e} + V_{ext}(\boldsymbol{r}) + \sum_{j}^{N} \left\langle \psi_j(\boldsymbol{r}') \middle| \frac{1}{|\boldsymbol{r} - \boldsymbol{r}'|} \middle| \psi_j(\boldsymbol{r}') \right\rangle \right] \psi_i(\boldsymbol{r}) - e^2 \sum_{i \neq j} \left\langle \psi_j(\boldsymbol{r}') \middle| \frac{1}{|\boldsymbol{r} - \boldsymbol{r}'|} \middle| \psi_j(\boldsymbol{r}') \right\rangle \psi_i(\boldsymbol{r}) = \epsilon_i \psi_i(\boldsymbol{r}). \quad (3.9)$$

The Hartree-Fock equation is generally not analytically solvable for more complex systems, but can be solved iteratively, in what is called a self-consistent field (SCF) calculation. Calculations start by making an initial guess for the orbitals, solving the HF equation to find approximate orbitals which are then used as the new initial guess. The method can then be repeated until the difference in the ground state energy obtained by two consecutive iterations is below a desired threshold, i.e., until the energy converges.

For a more detailed discussion of the HF scheme, and the upcoming DFT scheme, see Thijssen's book *Computational Physics* [21].

3.2 Density functional theory

In 1964 and 1965 two papers written by Hohenberg, Kohn and Sham were published in which a new method to solve the many body problem in quantum mechanics had been developed [26], [27]. This method, called density functional theory (DFT), have since seen tremendous success, awarding W. Kohn, together with J. A. People (who

extensively utilized DFT in the development of computational chemistry methods) the Noble Prize in Chemistry in 1998 [28]. And today, most electronic structure calculations, especially for solid-state materials, are based on DFT [21].

DFT ditches the many-body wavefunction approach taken in HF in favour of the electron density ($n(\boldsymbol{r})$), reducing the total degrees of freedom for a system of N electrons from $3N$ down to 3, regardless of the number of electrons.

Let's retrace our steps a bit here and lay the foundation for the DFT framework; by briefly examining the origins of the theory, and the importance of the two theorems Hohenberg and Kohn laid out in their initial paper.

3.2.1 DFT origins: The Thomas Fermi, and Thomas Fermi Dirac model

Shortly after E. Schrödinger introduced his Schrödinger wave equation, L. H. Thomas and E. Fermi constructed a semiclassical theory for the electronic structure of many-body systems [29], [30]. The Thomas Fermi model is based on the electron density, $n(\boldsymbol{r})$, rather than the wave function, $\psi(\boldsymbol{r})$, of such systems and can be regarded as a predecessor to DFT.

The accuracy of the Thomas Fermi model is limited, due to a couple key points. Firstly, the expression for the kinetic energy

$$T = \frac{3\hbar^2}{10\, m_e}(3\pi^2)^{\frac{2}{3}} \int [n(\boldsymbol{r})]^{\frac{5}{3}} d^3\boldsymbol{r}, \tag{3.10}$$

is an approximate term derived from the classical expression for kinetic energy of an electron. The Thomas Fermi model also does not consider either exchange energy or electron correlation. P. A. M. Dirac later added a term describing the exchange energy to the model. However, the resulting Thomas Fermi Dirac model still lacks sufficient accuracy when applied to realistic systems due to the approximate nature of the kinetic energy term and lack of any electron correlation [25].

The Thomas Fermi Dirac model, while not sufficiently accurate, shows that the electron density is a useful physical quantity for determining the properties of many-body systems. A notion which was fully realized in 1964 when Hohenberg and Kohn

released their paper, *Inhomogeneous electron gas*, in which they presented two crucial theorems of DFT [26].

3.2.2 The Hohenberg Kohn Theorems

Theorem 1. *Let $n(\boldsymbol{r})$ be the, possibly degenerate, ground state density for an N-electron system. Then $n(\boldsymbol{r})$ determines not only the electron number,*

$$N = \int n(\boldsymbol{r}) d^3\boldsymbol{r}, \tag{3.11}$$

but also, the external potential $V_{ext}(\boldsymbol{r})$ (i.e., there is a one-to-one correspondence between the ground state electron density and the external potential) and thus the Hamiltonian $\widehat{H}$ and thereby everything about this system (e.g., the ground- and excited-state wavefunctions. [31]

The first Hohenberg Kohn theorem states that the electron density (which expressed in terms of the many-body wavefunction can be written as) [25]

$$n(\boldsymbol{r}) = N \int \Psi^*(\boldsymbol{r}_1, \boldsymbol{r}_2, \dots, \boldsymbol{r}_N)\Psi(\boldsymbol{r}_1, \boldsymbol{r}_2, \dots, \boldsymbol{r}_N)\, d\boldsymbol{r}_2 \cdots d\boldsymbol{r}_N, \tag{3.12}$$

is uniquely defined given an external potential V_{ext}. This can be proven by a *reductio ad absurdum* argument, i.e., by proof of contradiction. The details of the proof are here left out, but one important implication of this theorem is that the ground state wavefunction can be written as a unique functional of the ground state electron density

$$\Psi_{GS} = \Psi[n(\boldsymbol{r})], \tag{3.13}$$

i.e., the electron density is sufficient to exactly describe a system. In fact, the one-to-one correspondence between the ground state electron density and the external potential allows the expectation value of any observable to be written as a unique functional of the ground state electron density, e.g., the total energy

$$E[n(\boldsymbol{r})] = \min_{\Psi|n} \left[\langle \Psi | \widehat{H} | \Psi \rangle\right], \tag{3.14}$$

where $\min_{\Psi|n}[\,]$ means that the expression in square brackets is minimized with respect to the wavefunctions consistent with the electron density.

Theorem 2. *There exists a universal functional of the density, $F[n(\boldsymbol{r})]$, such that for any N-representable density (i.e., any density that comes from some wavefunction for an N-electron system) $n(\boldsymbol{r})$, which yields a given number of electrons N, the energy functional is,*

$$E[n(\boldsymbol{r})] = F[n(\boldsymbol{r})] + \int n(\boldsymbol{r}) V_{ext}(\boldsymbol{r})\, d^3\boldsymbol{r} \geq E_{GS} \tag{3.15}$$

The equality holds when the density $n(\boldsymbol{r})$ is the, possibly degenerate, ground-state density for the external potential $V_{ext}(\boldsymbol{r})$ [31].

The universal functional described in Hohenberg and Kohn's second theorem is defined as follows:

$$F[n(\boldsymbol{r})] = \min_{\Psi|n} \left[\langle \Psi | \hat{F} | \Psi \rangle\right], \tag{3.16}$$

where $\hat{F}$ is all parts of the Hamiltonian that does not depend on the external potential, i.e.,

$$\hat{H} = \hat{F} + \hat{V}_{ext}. \tag{3.17}$$

Writing out the full energy functional yields

$$\begin{aligned} E[n(\boldsymbol{r})] &= \langle \Psi | \hat{H} | \Psi \rangle = \langle \Psi | \hat{F} | \Psi \rangle + \langle \Psi | \hat{V}_{ext} | \Psi \rangle \\ &= F[n(\boldsymbol{r})] + \int n(\boldsymbol{r}) V_{ext}(\boldsymbol{r})\, d^3\boldsymbol{r} \geq E_{GS}. \end{aligned} \tag{3.18}$$

Letting the wavefunction be the ground state wavefunction thus yields

$$\langle \Psi_{\mathrm{GS}} | \hat{H} | \Psi_{\mathrm{GS}} \rangle \geq E_{GS}. \tag{3.19}$$

But

$$\langle \Psi_{\mathrm{GS}} | \hat{H} | \Psi_{\mathrm{GS}} \rangle = E_{GS}, \tag{3.20}$$

by definition. Thus, the wavefunction consistent with the electron density that minimizes the energy functional must be the ground state wavefunction. Taken the other way around, the electron density that minimizes the energy functional must be the true electron density of the ground state.

While the Hohenberg Kohn theorems put DFT on solid theoretical ground, they provide no practical method with which to calculate a systems ground state electron density.

For such a method, we must turn to the Kohn Sham equations, first presented in 1965 by Kohn and Sham in their paper "*Self-Consistent Equations Including Exchange and Correlation Effects"* [27].

3.2.3 The Kohn Sham Equations

From the Hohenberg Kohn theorems we know that the energy functional can be written as

$$E[n(\boldsymbol{r})] = F[n(\boldsymbol{r})] + \int n(\boldsymbol{r}) V_{ext}(\boldsymbol{r})\, d^3\boldsymbol{r}, \tag{3.21}$$

where $F[n(\boldsymbol{r})]$ includes every part of the Hamiltonian that does not depend on the external potential. Let us first consider the case of non-interacting particles. Here we only deal with kinetic energy (besides the external potential), thus

$$E[n(\boldsymbol{r})] = T[n(\boldsymbol{r})] + \int n(\boldsymbol{r}) V_{ext}(\boldsymbol{r})\, d^3\boldsymbol{r}. \tag{3.22}$$

Using the method of Lagrange multipliers and letting $E[n(\boldsymbol{r})]$ vary with respect to $n(\boldsymbol{r})$ yields

$$\frac{\delta T[n(\boldsymbol{r})]}{\delta n(\boldsymbol{r})} + V_{ext} = \lambda n(\boldsymbol{r}), \tag{3.23}$$

where λ is the Lagrangian multiplier associated with the constraint that variations to the electron density must yield the correct total number of electrons (i.e., the total number of electrons must remain the same) [21]. We know from previous discussion of the HF method that for non-interacting electrons, the ground state wavefunction can be represented by a Slater determinant in which the single particle wavefunctions (i.e., the orbitals) each satisfy the single-particle Schrödinger equation

$$\left[-\frac{\nabla^2}{2} + V_{ext}(\boldsymbol{r})\right]\psi_i(\boldsymbol{r}) = \epsilon_i \psi_i(\boldsymbol{r}). \tag{3.24}$$

The ground state electron density can then be constructed from the orbitals according to:

$$n(\boldsymbol{r}) = \sum_{i=1}^{N} |\psi_i(\boldsymbol{r})|^2. \tag{3.25}$$

If we instead consider a many-body system where we allow for electron interactions, we may write the energy functional as follows:

$$E[n(\boldsymbol{r})] = T[n(\boldsymbol{r})] + \int n(\boldsymbol{r}) V_{ext}(\boldsymbol{r})\, d^3\boldsymbol{r} + \frac{1}{2}\int d^3\boldsymbol{r} \int \frac{n(\boldsymbol{r}) n(\boldsymbol{r}')}{|\boldsymbol{r} - \boldsymbol{r}'|} d^3\boldsymbol{r}' + E_{xc}[n(\boldsymbol{r})]. \tag{3.26}$$

The first three terms in (3.26) are the kinetic energy of non-interacting electrons, the energy due to the external potential, and the electrostatic Coulomb energy (also called the Hartree energy). The last term represents the exchange correlation energy and is, by definition, given by all contributions not accounted for in the first three terms.

Varying equation (3.26) with respect to the electron density yields

$$\frac{\delta T[n(\boldsymbol{r})]}{\delta n(\boldsymbol{r})} + V_{eff} = \lambda n(\boldsymbol{r}), \tag{3.27}$$

where

$$V_{eff} = V_{ext} + \frac{\delta E_{ex}[n(\boldsymbol{r})]}{\delta n(\boldsymbol{r})} + \int \frac{n(\boldsymbol{r}')}{|\boldsymbol{r} - \boldsymbol{r}'|} d^3\boldsymbol{r}', \tag{3.28}$$

is called the effective potential. Exchanging V_{eff} with V_{ext} in (3.27) exactly yields (3.23), i.e., the two equations are on the same form. Thus, as was the case for (3.23), an analogue set of one-electron Schrödinger equations can be found:

$$\left[-\frac{\nabla^2}{2} + V_{eff}(\boldsymbol{r})\right]\psi_i(\boldsymbol{r}) = \epsilon_i \psi_i(\boldsymbol{r}). \tag{3.29}$$

These single-particle equations (3.29) are called the Kohn-Sham (KS) equations, and the solutions ψ_i are called Kohn-Sham (KS) orbitals, from which the electron density can be built up according to:

$$n(\boldsymbol{r}) = \sum_{i=1}^{N} |\psi_i(\boldsymbol{r})|^2. \tag{3.30}$$

It is worth pointing out that neither the KS orbitals ψ_i, nor their energies ϵ_i, describe real electron states, but rather fictitious, non-interacting, single-particle states, and their energies.

Even though it mathematically makes little sense to relate the KS orbitals to those of real electrons, there is multitude of experimental evidence indicating that they are quite reasonable descriptions of electron states [25]. Individual orbital energies can however, in general, not be associated with any excitation. The sum of all orbital energies is on the other hand related to the total ground state energy in following way:

$$E = \sum_{i=1}^{N} \epsilon_i - \frac{1}{2}\int \frac{n(\boldsymbol{r})n(\boldsymbol{r}')}{|\boldsymbol{r}-\boldsymbol{r}'|} d^3\boldsymbol{r}\, d^3\boldsymbol{r}' - \int n(\boldsymbol{r})\, V_{xc}[n(\boldsymbol{r})] + E_{xc}[n(\boldsymbol{r})]. \tag{3.31}$$

where V_{xc} is the exchange correlation potential given by

$$V_{xc} = \frac{\delta E_{xc}[n(\boldsymbol{r})]}{\delta n(\boldsymbol{r})}. \tag{3.32}$$

The derivation of the Kohn-Sham equations in principle does not invoke any approximations and DFT as a method is thus exact. However, the exact form of the exchange correlation functional $E_{ex}[n(\boldsymbol{r})]$ is not known, even for a uniform electron gas, forcing practitioners of DFT to employ approximations when carrying out calculations.

3.2.4 Exchange-correlation and approximations

As the name suggests, the exchange-correlation energy is really comprised of two parts, exchange, and correlation:

$$E_{xc}[n(\boldsymbol{r})] = E_x[n(\boldsymbol{r})] + E_c[n(\boldsymbol{r})]\,. \tag{3.33}$$

Exchange energy is explicitly accounted for in HF theory, however, in DFT the exchange functional, while exact in nature, is unknown (in fact both the exchange and correlation functionals are exact but unknown in DFT). Moreover, the exchange and correlation contributions are in general mixed up and difficult to separate. The exchange-correlation energy must therefore be approximated, and can be done in a variety of ways, of which the local density approximation (LDA) is the simplest.

In the LDA, as the name suggests, the exchange-correlation functional is assumed to depend locally on the electron density, and is given by

$$E_{xc}[n(\boldsymbol{r})] = \int \epsilon_{xc}[n] n(\boldsymbol{r}) d\boldsymbol{r}, \tag{3.34}$$

where $\epsilon_{xc}[n]$ is the exchange-correlation energy per unit volume of a homogenous electron gas whose density is given by $n(\boldsymbol{r})$. The LDA works surprisingly well for many solid-state materials but tend to overestimate the binding of atoms, producing too short bond-distances and lattice parameters [32].

The generalised gradient approximation (GGA), in which the exchange-correlation functional not only depends on the local electron density $n(\boldsymbol{r})$, but also on its gradient $\nabla n(\boldsymbol{r})$, tries to improve on the LDA. GGA have been shown to improve accuracy, particularly for molecular systems [33], but is not some magic bullet, and GGA functionals (depending on the parametrization) will not always outperform LDA functionals for all types of systems.

Meta-GGA is the next step beyond GGA on the Jacob's ladder, see Figure 3.1, and incorporates the Laplacian (second order derivative, $\nabla^2 n(\boldsymbol{r})$) in the description of the exchange-correlation functional [34].

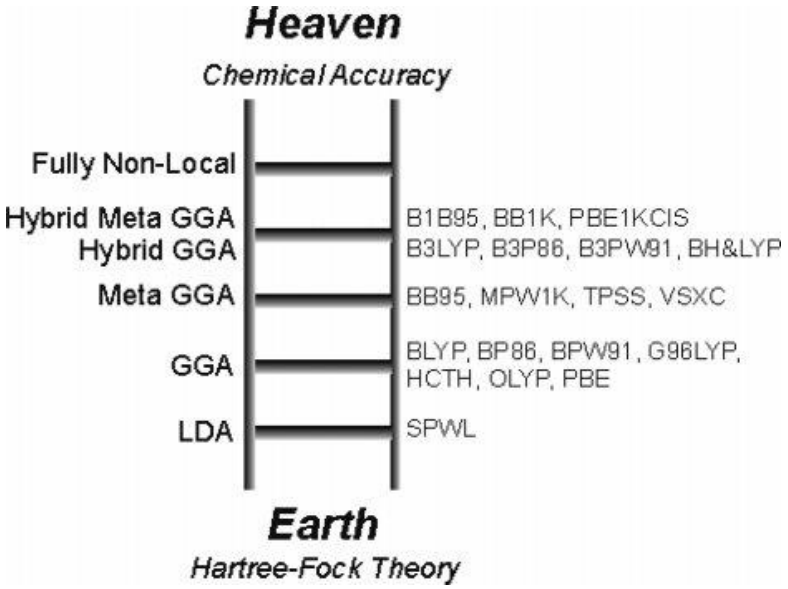

Figure 3.1. Jacob's ladder of DFT approximations for the exchange-correlation energy. To the right side of the ladder, common functionals for the respective rungs are listed [35].

Taking one step further up the rungs of Jacob's ladder we find Hybrid GGA and Hybrid Meta GGA functionals. These functionals do in some ($< 100\%$) or even full (100%) capacity incorporate HF (exact) exchange. The ideal amount of HF exchange to

incorporate for a given functional cannot be calculated from first principles, so hybrid functionals always have some form of empiricism built in (commonly by fitting obtained values with respect to experimental data for selected properties, e.g., total energy or electron affinity, for a set of materials). Although hybrid functionals show modest improvements over GGA and LDA for solid-state materials, significant improvements have been shown for predicting molecular properties [35].

Two functionals have been used in this work, M06-D3 and TPSSh. Both being of the Hybrid Meta GGA type.

M06-D3 is in the Minnesota family of functionals; a suite of functionals developed by Prof. Donald Truhlar's group at the University of Minnesota. M06-D3 is based on the versatile M06 functional which is a non-local (global) functional with 27% HF exchange, intended for main group thermochemistry [36]. The D3 part of the name comes from the Grimme dispersion correction added to the functional for improved accuracy for modelling long range dispersion forces (e.g., van der Waal forces) [37], [38].

TPSSh is a continuation on the Meta-GGA functional TPSS, improving on it by including 10% HF exchange. TPSSh have been proven to produce structures of similar quality to those obtained using the common B3LYP functional (Hybrid Meta-GGA); and has been shown to also achieve improved accuracy in estimated energies compared to the same functional [39].

3.2.5 Time-Dependent DFT

The original DFT framework, as derived by Hohenberg, Kohn and Sham, is time-independent in its formulation (the Hohenberg Kohn theorems only holds for electron densities describing time-independent ground states). Runge and Gross extended the DFT framework into the time-dependent domain in 1984 by showing that the one-to-one correspondence between an external potential and the electron density holds even for time-dependent external potentials [40].

Being able to apply DFT to time-dependent potentials extends the application of the theory to include computation of properties such as excited states and frequency-

dependent polarizability [41]; and Time-dependent DFT (TD-DFT), have seen particular success in calculations of optical properties such as molecular absorption spectra [25].

4 Experimental

Figure 4.1 show a flowchart depicting how data acquisition on the Y5 and PF5-Y5 molecules was carried out.

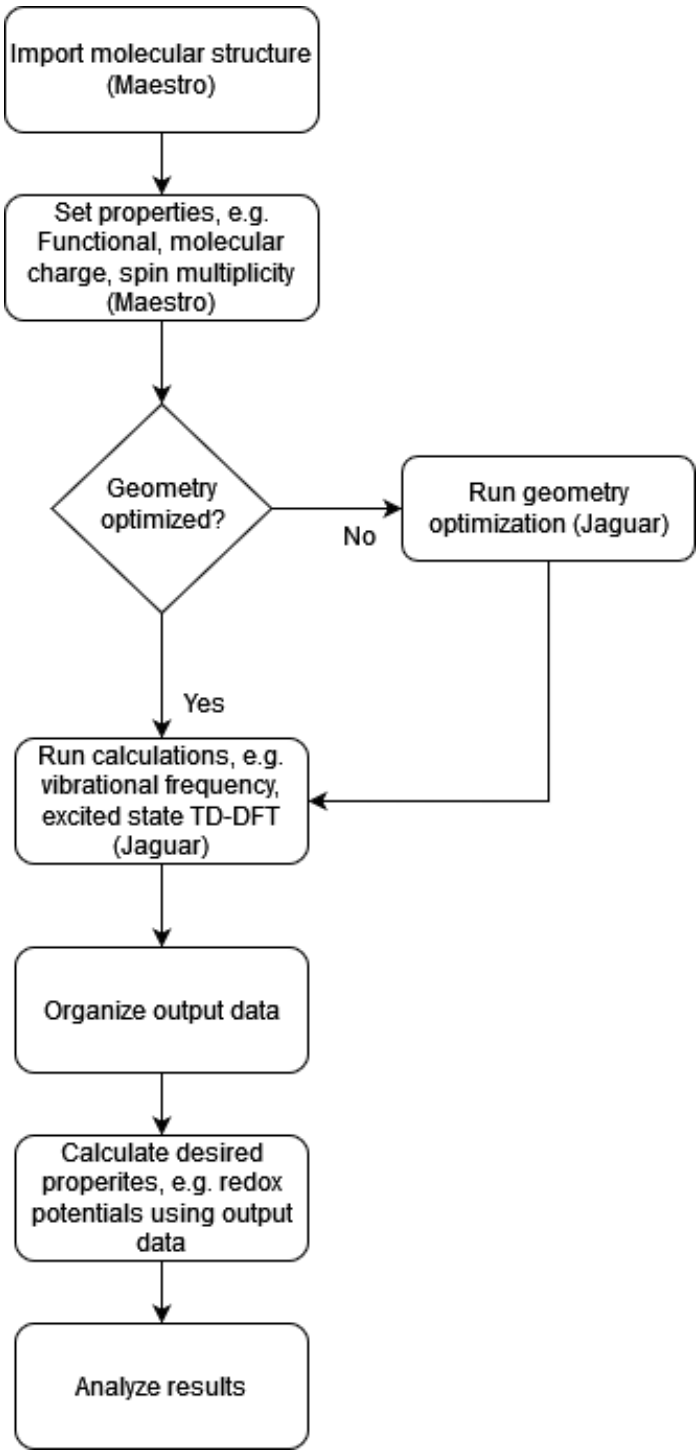

Figure 4.1. Flowchart illustrating the working procedure from start to finish for acquiring data on the Y5 and PF5-Y5 molecules. Objects in (parentheses) indicate which program was used for that step.

All calculations were carried out on the Tetralith high performance computation (HPC) cluster which is the largest HPC cluster at the national supercomputer centre (NSC) at Linköping University [42]. Calculations were performed using the Schrödinger software platform [43], using Maestro (release 2020-4) for modelling, and manipulating the molecular structures as well as visualizing certain types of data (e.g., absorption spectra), and Jaguar (version 11.0 release 144) for the ab initio quantum mechanical calculations (all done within the DFT and TD-DFT framework). Data from the Jaguar output files was organized and analysed in either Microsoft excel (Version 2111 Build 16.0.14701.20204) or MATLAB (release R2019b).

4.1 Computational details

Geometry optimization was carried out in vacuum using the M06-D3 functional and 6-311G** basis set. Single point energy calculations, both in vacuum and in chlorobenzene solution (implemented using the implicit Conductor-like polarizable continuum model (CPCM) [44]), were carried out using two different functionals, M06-D3 and TPSSh; and again, for both functionals, the 6-311G** basis set was used. Vibrational frequency calculations were carried out using the M06-D3 and TPSSh functionals, but due to the high computational cost of these calculations, the smaller 6-31G* basis set was used.

The full Gibbs free energy G was constructed for each species (neutral, oxidized, and reduced, each at their own optimized geometry, as well as oxidized and reduced species at the geometry of the optimized neutral molecule) of the Y5 and PF5-Y5 molecules by summing up all contributions:

$$G = E_{SCF} + E_{ZPT} + pV + U_{vib} + U_{rot} + U_{trans} - (S_{vib} + S_{rot} + S_{trans}), \quad (4.1)$$

where the subscripts in (4.1) represent the following:

- **SCF:** The total energy (Nuclear repulsion + electronic energy + energy corrections). Obtained from self-consistent field DFT calculations (single point energy).

- **ZPT**: The zero-point energy (lowest possible energy for a given quantum mechanical system). Obtained from vibrational frequency calculations as the vibrational internal energy at $T = 0\,K$.
- **Vib, rot, trans**: The vibrational, rotational, and translational energies of the molecule, i.e., all thermal energy contributions. Obtained from vibrational frequency calculations at $T > 0\,K$ (For this thesis, $T = 298.15\,K$ and $P = 1\,atm$ have been used for all calculations).

It should be noted that the addition/removal of one electron required to create ions from neutral molecules result in a different spin multiplicity for the neutral and ionic species. Calculations on the neutral molecules (singlet state, i.e., spin multiplicity = 1) have been performed using a restricted spin treatment. Meanwhile, calculations on all ionized molecules (doublet state, i.e., spin multiplicity = 2) have been computed using an unrestricted spin treatment.

Using an unrestricted spin treatment runs the risk of spin contamination (artificial mixing of spin-states), however, running restricted spin-treatment calculations can have considerable increases in computational cost in order to correctly deal with both single and double occupied orbitals and their interaction [45].

A set of restricted spin treatment calculations was run on the ionic states that had the largest deviation ($< 7.5\%$) in expected total spin $\langle S^2 \rangle$, i.e., showed most signs of being spin contaminated. The total difference in Gibbs free energy between the restricted and unrestricted calculations was less than 0.0001%. Considering the negligible effects on the total Gibbs free energy, no further treatment of spin contamination was implemented.

Values for the HOMO and LUMO energies for both Y5 and PF5-Y5 have previously been experimentally estimated using redox potentials obtained from cyclic voltammetry [2] (i.e., the HOMO and LUMO energies are simply obtained as the oxidation and reduction potentials with respect to the vacuum level). Thus, the Born-Haber thermodynamic cycle (see Figure 4.2) have been employed to calculate the redox potentials and estimate the HOMO and LUMO energies.

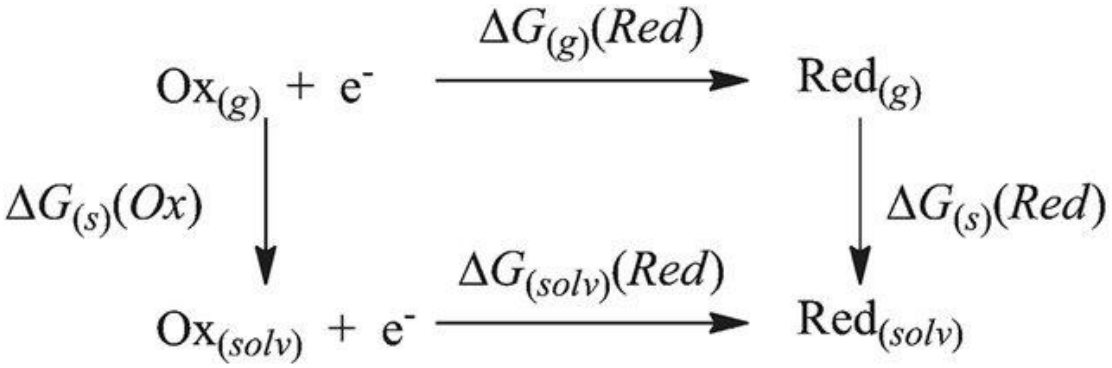

Figure 4.2. Representation of the Born-Haber thermodynamic cycle [46]. Ox and Red are short for oxidized and reduced respectively. (g) means that the species is in gas phase, (solv) means that the species is in solvation. (s) means solution and is used when representing a species change in Gibbs free energy ΔG when going between (g) and (solv).

The reduction potential Φ_{Red} and oxidation potential Φ_{Ox} are evaluated using (2.4) and (2.5) respectively, repeated here in their combined form:

$$\Phi_{\mathrm{Red/Ox}} = -\frac{\Delta G_{(solv)}(Red)}{nF}, \tag{4.2}$$

in which $\Delta G_{(solv)}(Red)$ is calculated from following expression:

$$\Delta G_{(solv)}(Red) = \Delta G_{(g)}(Red) + \Delta G_{(s)}(Red) - \Delta G_{(s)}(Ox). \tag{4.3}$$

Here, $\Delta G_{(g)}(Red)$ is obtained as the difference in the Gibbs free energy (4.1) between the involved redox pairs (reduced/neutral for Φ_{red} and neutral/oxidized for Φ_{Ox}) in gas-phase. $\Delta G_{(s)}(Red)$ and $\Delta G_{(s)}(Ox)$ are the differences in total Gibbs free energy between the molecules in gas-phase and in solution, for the reduced and oxidized species respectively, and are directly obtained from the single point energy calculations in solution.

The fundamental electrochemical gap is calculated using (2.6), repeated here for convenience:

$$E_{fund} = \Phi_{Red} - \Phi_{Ox}, \tag{4.4}$$

and the oxidation and reduction energy (energy required to overcome the potentials) are given by the negative of the redox potentials:

$$E_{Red} = -\Phi_{Red}, \tag{4.5}$$

$$E_{Ox} = -\Phi_{Ox}. \tag{4.6}$$

Three cases have been considered when calculating the redox potentials (and accompanying fundamental gap):

1. **Full (including all effects):** By constructing the full Gibbs free energy for the neutral and ionized states in their respective relaxed geometry.
2. **Adiabatic (only including relaxation):** By constructing Gibbs free energy (excluding thermal contributions) on the neutral and ionized states in their respective relaxed geometry.
3. **Vertical (excluding both thermal and relaxation effects):** By constructing Gibbs free energy (excluding thermal contributions) on the neutral and ionized states, all in the geometry of the optimized neutral state.

Further sets of estimated redox potentials have been obtained by the built in optoelectronic properties calculation protocol (abbreviated as "OptoP protocol" moving forward) as implemented in Jaguar [47]. The OptoP protocol have two methods with which optoelectronic properties such as redox potentials, hole and electron recombination energies, and triplet energy can be calculated.

The first, and computationally most cost-effective method, called the Koopman approximation, finds the redox potentials by optimizing the neutral molecule in its ground state and performing a single point energy calculation to find the orbital energies. The redox potentials are then found according to

$$\Phi_{Red/Ox} = slope \cdot E_{orbital} + intercept, \tag{4.7}$$

where the slope ($-17.50\,V$ for oxidation and $-22.50\,V$ for reduction) and intercept ($-2.17\,V$ for oxidation and $-3.21\,V$ for reduction) values are obtained from linear regression against a dataset consisting of experimentally obtained redox potentials over a wide range of OLED materials. The dataset is calibrated for the B3LYP functional and MIDI! basis set (computationally cost-efficient small basis set with similar performance to 6-31G* [48]), thus both geometry optimization and single point energy calculations were performed using B3LYP + MIDI!.

The estimated oxidation and reduction energies are obtained from the redox potentials as follows:

$$Absolute_{Electrode} = E_{NHE} + \Phi_{electrode} \quad (4.8)$$

$$E_{Red/Ox} = Absolute_{Electrode} - \Phi_{Red/Ox}. \quad (4.9)$$

Using the normal hydrogen electrode ($\Phi_{NHE} = -E_{NHE}$) as reference electrode simplifies (4.8) and (4.9), yielding

$$Absolute_{Electrode} = E_{NHE} - E_{NHE} = 0 \quad (4.10)$$

$$E_{Red/Ox} = -\Phi_{Red/Ox}. \quad (4.11)$$

The OptoP protocol's secondary method, called the adiabatic method, calculates the redox potentials as follows:

$$\Phi_{Ox} = -(E_{electrode} + E_{electron} + E_{ion} - E_{neutral}) \quad (4.12)$$

$$\Phi_{Red} = -(E_{electrode} - E_{electron} + E_{ion} - E_{neutral}). \quad (4.13)$$

where $E_{electron}$ is taken as $-4.28\ eV$ [47]. The adiabatic method calculations are performed on both the (N)-electron neutral molecule as well as the $(N \pm 1)$-electron ions in their respective optimized geometries (hence why it is called the adiabatic method). The adiabatic method works from first principles and is thus not optimized for any specific functional or basis set. The same functional (M06-D3) and basis set (6-311G**) that was used for single point energy calculations was therefore used for the adiabatic approach as well.

As this method in theory provides no new information (as long as one chose the electrode such that it cancels the $E_{electron}$ term, i.e., $E_{electrode} = E_{NHE} = -E_{electron}$) compared to performing single point energy calculations on neutral and ionic states, the data obtained from this method simply serves as a double check to the values obtained by constructing the Gibbs free energy (excluding thermal contributions) of the relaxed species.

Vertical transition energies were calculated using TDDFT (both in gas-phase and in solution) using the same functionals (M06-D3 and TPSSh) and basis-set (6-311G**) as for single point energy calculations. Optical absorption spectra were obtained by constructing stick-spectrum from the vertical transition energies and dressing them in a convolution of Gaussian line shapes. The optical gap was taken as the energy of the first optically allowed electronic transition.

5 Results & Discussion

5.1 Energy levels

Calculated redox potentials are given in Table 5.1. 1F5, 2F5 and 3F5 represent oligomers (# = number of monomers) of PF5-Y5. The computational cost of frequency calculations for structures larger than 1F5-Y5 exceeded what could be simulated. Only values for 2F5-Y5 (accounting for all effects) calculated using the OptoP method are therefore present. Similarly, only values for 3F5-Y5 obtained using the OptoP method are present because geometry optimization using M06-D3 was unsuccessful on that structure.

Table 5.1. Redox potentials and fundamental gap for Y5 and PF5-Y5 in chlorobenzene solution, when accounting for various effects.*Experimental data is from [2] and was obtained using cyclic voltammetry.

Molecule	Functional	Effects	$-\Phi_{red}(eV)$	$-\Phi_{Ox}\ (eV)$	$E_{fund}(eV)$
Y5	Experimental*	All	-5.56	-3.89	1.67
PF5-Y5	Experimental*	All	-5.52	-3.84	1.68
Y5	M06-D3	All	-5.54	-3.75	1.79
Y5	TPSSh	All	-5.25	-3.58	1.67
Y5	MIDI!	All	-5.67	-3.87	1.80
1F5-Y5	M06-D3	All	-5.39	-3.78	1.61
1F5-Y5	TPSSh	All	-4.86	-3.67	1.19
1F5-Y5	MIDI!	All	-5.46	-3.84	1.62
2F5-Y5	MIDI!	All	-5.48	-3.87	1.61
3F5-Y5	MIDI!	All	-5.46	-3.88	1.58
Y5	M06-D3	Adiabatic	-5.59	-3.63	1.95
Y5	TPSSh	Adiabatic	-5.27	-3.50	1.77
1F5-Y5	M06-D3	Adiabatic	-5.55	-3.67	1.89
1F5-Y5	TPSSh	Adiabatic	-5.00	-3.47	1.53
2F5-Y5	M06-D3	Adiabatic	-5.55	-3.45	2.09
Y5	M06-D3	Vertical	-5.66	-3.54	2.12
Y5	TPSSh	Vertical	-5.30	-3.35	1.95
1F5-Y5	M06-D3	Vertical	-5.63	-3.49	2.13
2F5-Y5	M06-D3	Vertical	-5.60	-3.50	2.10

From Table 5.1, the choice of functional (i.e., the description of the exchange-correlation interaction) can be seen to significantly impact obtained values. TPSSh consistently yields higher values for the redox potentials compared to those obtained using M06-D3 or experimentally, as illustrated in Figure 5.1 and Figure 5.2.

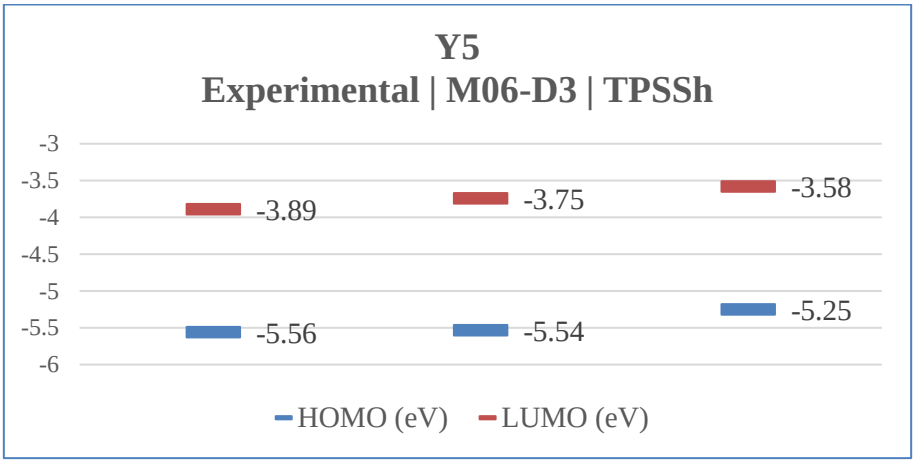

Figure 5.1. Energy level diagram of Y5, highlighting the difference between the M06-D3 and TPSSh functionals.

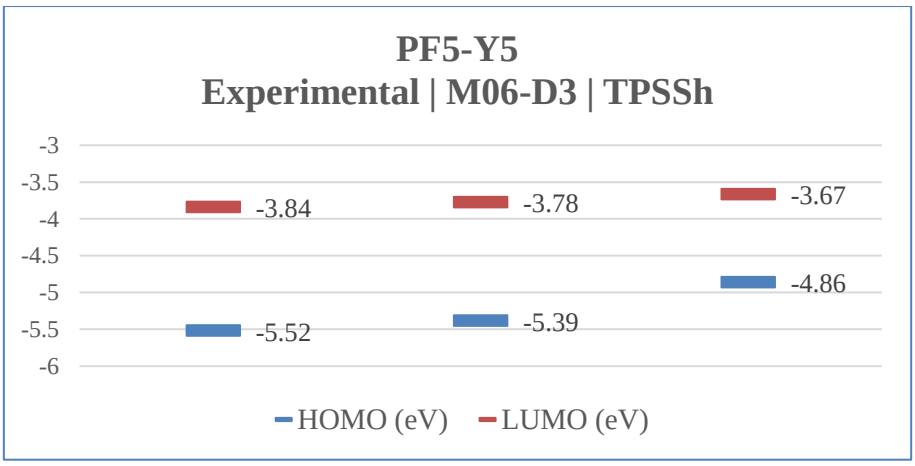

Figure 5.2. Energy level diagram of PF5-Y5, highlighting the difference between the M06-D3 and TPSSh functionals. *Experimental values are from neat films. As such, oligomer length may vary. Computed values are from 1F5-Y5.

Both oxidation and reduction energies calculated using M06-D3 agree reasonably well with experimental values for both Y5 and PF5-Y5; and the resulting differences in the fundamental gap are $\Delta E = 0.12\ eV$ for Y5 and $\Delta E = 0.06$ eV for PF5-Y5.

TPSSh always yields higher energies than what was found experimentally. The oxidation energy of PF5-Y5 is a particularly poor fit, being $0.66\ eV$ higher, resulting in a difference of $\Delta E = 0.49\ eV$ for the fundamental gap. The calculated gap for Y5

turns out to perfectly match the experimental value, however, both oxidation and reduction energies are significantly overestimated (0.31 eV).

The effects of relaxation, as well as the effects of thermal contributions, is illustrated in Figure 5.3 and Figure 5.4 for Y5 and PF5-Y5 respectively.

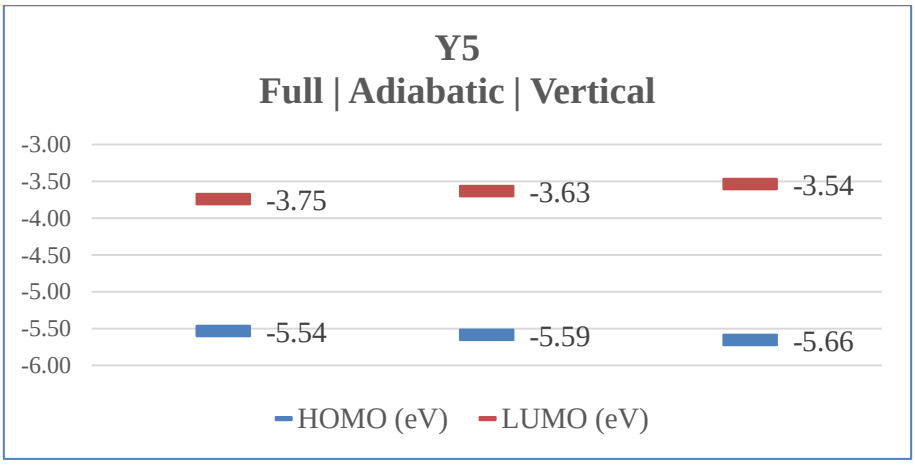

Figure 5.3. Energy level diagram for Y5 using different approximations for the fundamental gap. Data obtained using M06-D3.

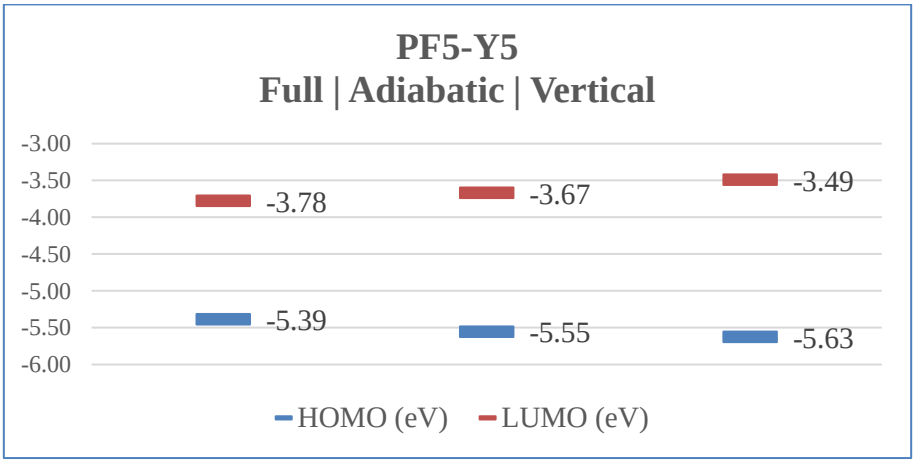

Figure 5.4. Energy level diagram for PF5-Y5 (1F5-Y5) using different approximations for the fundamental gap. Data obtained using M06-D3.

Both relaxation and thermal contributions act to lower the reduction energy and raise the oxidation energy, which consequently also lowers the fundamental gap for both Y5 and PF5-Y5. The total gap reduction going from the vertical transition approximation to accounting for all effects equates to a total difference of $\Delta E = 0.42$ eV for Y5, and $\Delta E = 0.52$ eV for PF5-Y5.

The adiabatic approximation proves to be a good middle ground, having $\Delta E = 0.16\ eV$ (for Y5) and $\Delta E = 0.28\ eV$ (for PF5-Y5) when compared to including all effects, while only modestly increasing the computational cost over the vertical transition approach (as two more geometry optimizations must be run, taking roughly a couple of hours each on Tetralith if performed on 1F5-Y5). For reference, the fundamental gap requires three vibrational frequency calculations, which, even on a high-performance computational cluster like Tetralith, take roughly 3 days to calculate each (for 1F5-Y5). Meanwhile, a single point calculation required for the vertical approximation takes roughly 45 minutes on the same molecule.

The effects that the oligomer length has on the fundamental gap is illustrated in Figure 5.5. As the oligomer length increases from one unit to two repeating units, the gap decreases by $0.01\ eV$, and further when oligomer length goes from two to three units, the gap reduces by another $0.03\ eV$.

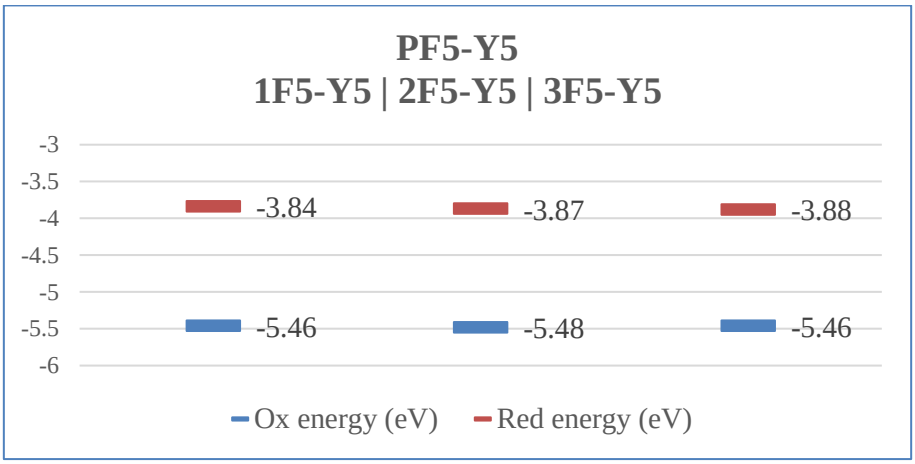

Figure 5.5. Energy level diagram for PF5-Y5, showcasing the effects of oligomer length. Data obtained using the OptoP protocol.

5.2 Absorption spectra

The absorption spectra for Y5 and PF5-Y5 in chlorobenzene solution, obtained using M06-D3, can be seen in Figure 5.6, and the same spectrum obtained using TPSSh can be seen in Figure 5.7.

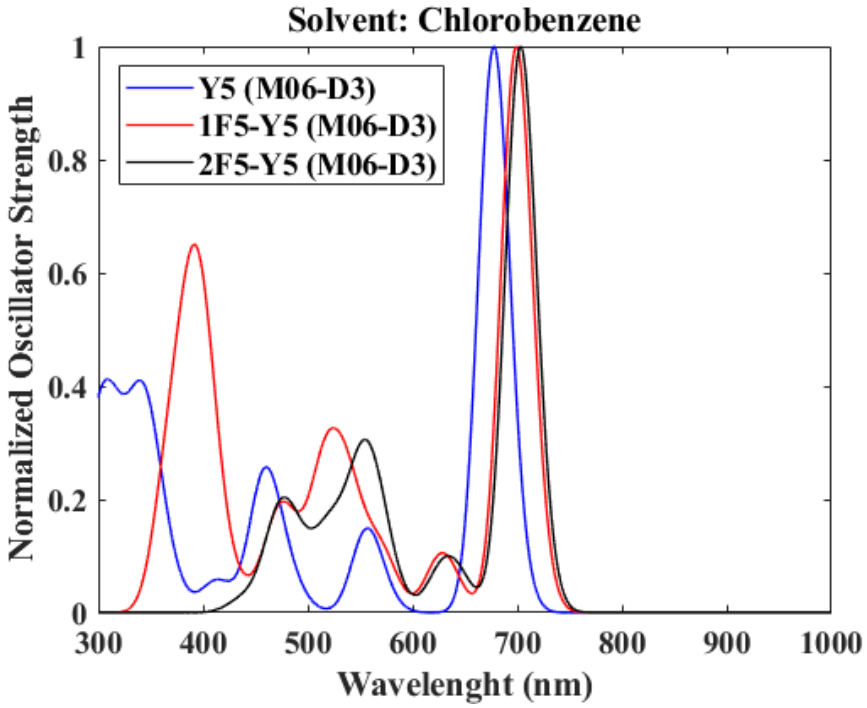

Figure 5.6. Normalized absorption spectra of Y5 and PF5-Y5 (1F5-Y5 and 2F5-Y5) in chlorobenzene solution obtained using the M06-D3 functional, constructed from 50 vertical transitions dressed in Gaussian line shapes (half-bandwidth = 30 nm).

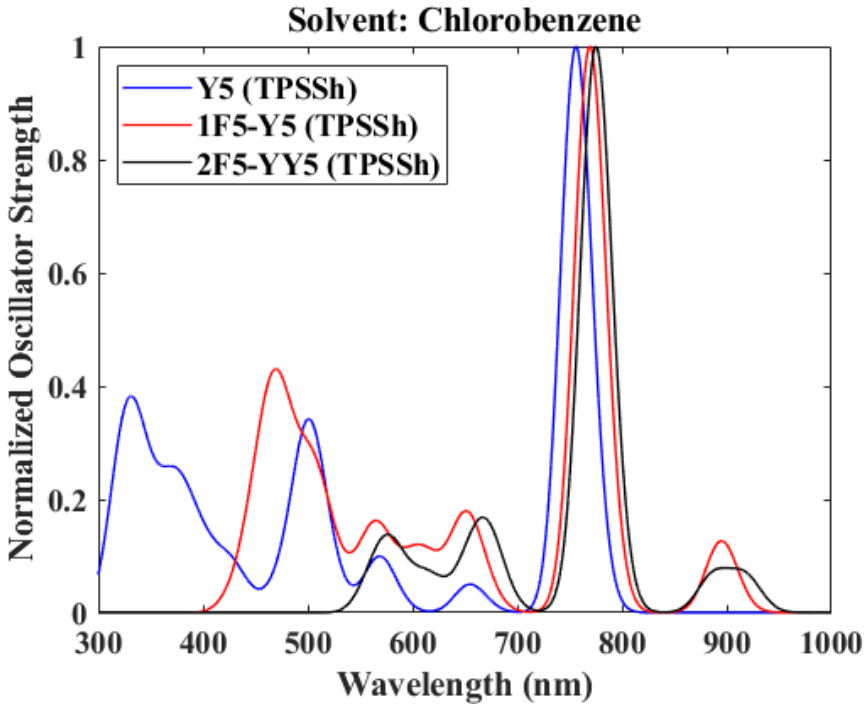

Figure 5.7. Normalized absorption spectra of Y5 and PF5-Y5 (1F5-Y5 and 2F5-Y5) in chlorobenzene solution obtained using the TPSSh functional, constructed from 50 vertical transitions dressed in Gaussian line shapes (half-bandwidth = 30 nm). **NOTE:** the apparent low absorbance of 2F5-Y5 below ~550 nm is an artifact caused by only considering 50 transitions.

General features of the absorption spectra obtained using TPSSh agree well with experimentally obtained spectra, see Figure 5.8; however, the peaks are slightly redshifted across all wavelengths. Absorption spectra obtained using M06-D3 are blueshifted across all wavelengths compared to both the experimental spectra and the spectra obtained using TPSSh; and the peak around $900\,nm$ which is present in the TPSSh spectra, is not present in the M06-D3 one. Furthermore, the calculated absorption spectra, for both M06-D3 and TPSSh, show that the absorptions become more redshifted as the oligomer length increases. However, since absorption spectra has only been obtained for two oligomer lengths (1F5 and 2F5), more data (i.e., longer oligomers: 3F5, 4F5 or even 5F5) would increase the certainty of the results.

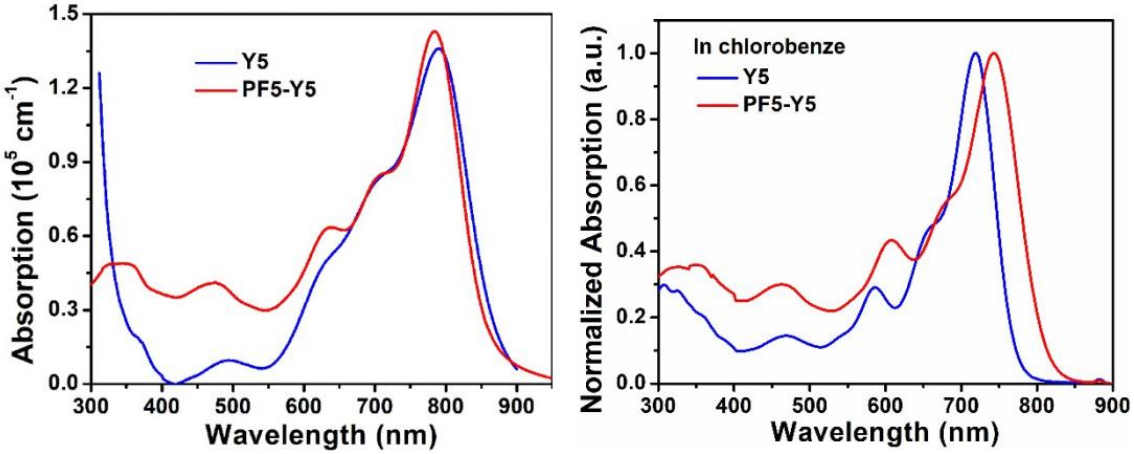

Figure 5.8. Normalized absorption spectra of Y5 and PF5-Y5 in neat films (left image) and in chlorobenzene solution (right image). Data taken from [2] (supplemental information).

Absorption spectra for Y5 in gas-phase and in solution (chlorobenzene) is illustrated in Figure 5.9. The entire spectrum for Y5 in chlorobenzene is redshifted compared to Y5 in gas-phase, and the amount of redshift increases with increasing wavelength. The main peak in gas-phase is located at $691\,nm$, and in solution at $756\,nm$, giving a maximum redshift of $65\,nm$. Similar redshifts were obtained across all absorption spectra for all molecules.

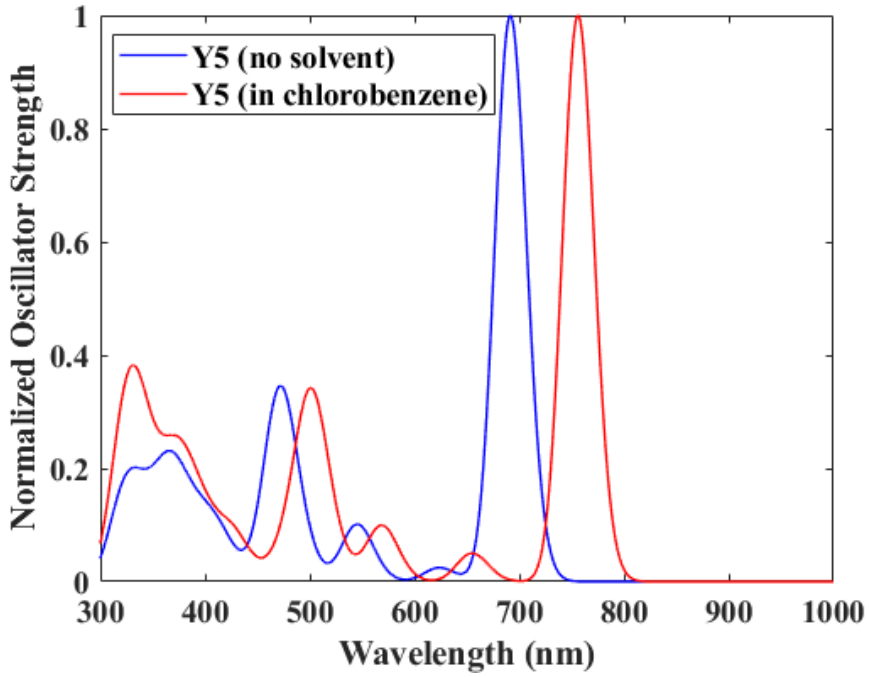

Figure 5.9. Normalized absorption spectra of Y5 in gas-phase (no solution) and in chlorobenzene solution, constructed from 50 vertical transitions dressed in Gaussian line shapes (half-bandwidth = 30 nm). The functional TPSSh was used for both curves.

Effects on the absorption spectrum due to Y5 and PF5-Y5 forming dimers can be seen in Figure 5.10 and Figure 5.11 respectively. The main peak for both the Y5 and PF5-Y5 dimers are blueshifted compared to their single molecule counterparts, with a larger blueshift for the PF5-Y5 dimer. Another aspect is the emergence of a shoulder slightly below the main peak for both dimer spectra. This shoulder is even more pronounced in the experimentally obtained spectra. It therefore seems likely that dimer stacking, or other forms of agglomeration or aggregation, plays an important role in both Y5 and PF5-Y5-based devices. Furthermore, both the spectra for the Y5 and PF5-Y5 dimers show small peaks at higher wavelengths (above the main peaks) compared to the non-dimer spectra. Thus, even though the main peaks of the dimers are slightly blueshifted, the first allowed transitions, and therefore also the exciton binding energy, is lower.

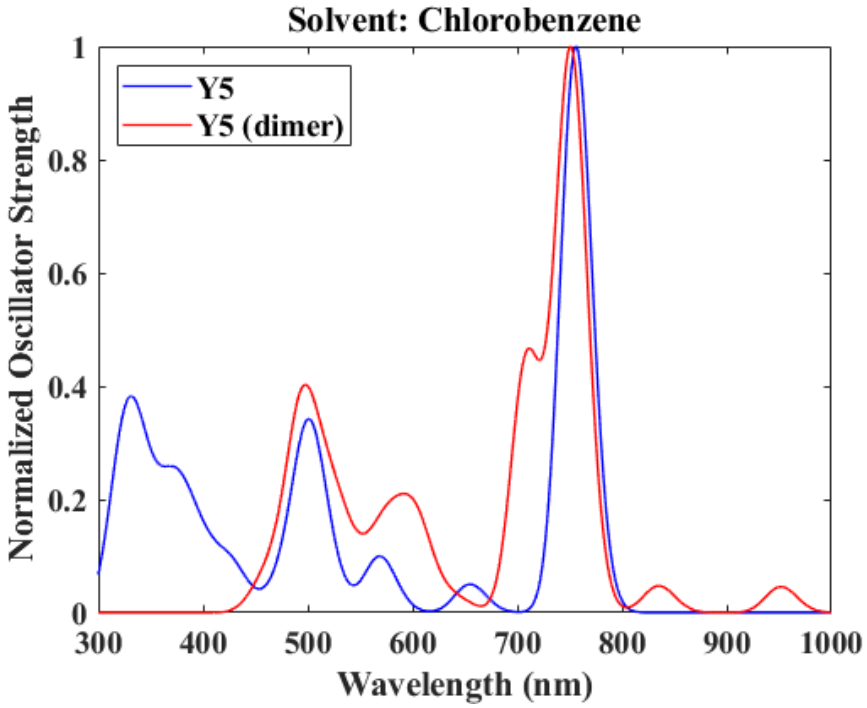

Figure 5.10. Normalized absorption spectra of Y5 and its dimer in chlorobenzene solution, constructed from 50 vertical transitions dressed in Gaussian line shapes (half-bandwidth = 30 nm). The functional TPSSh was used for both curves.

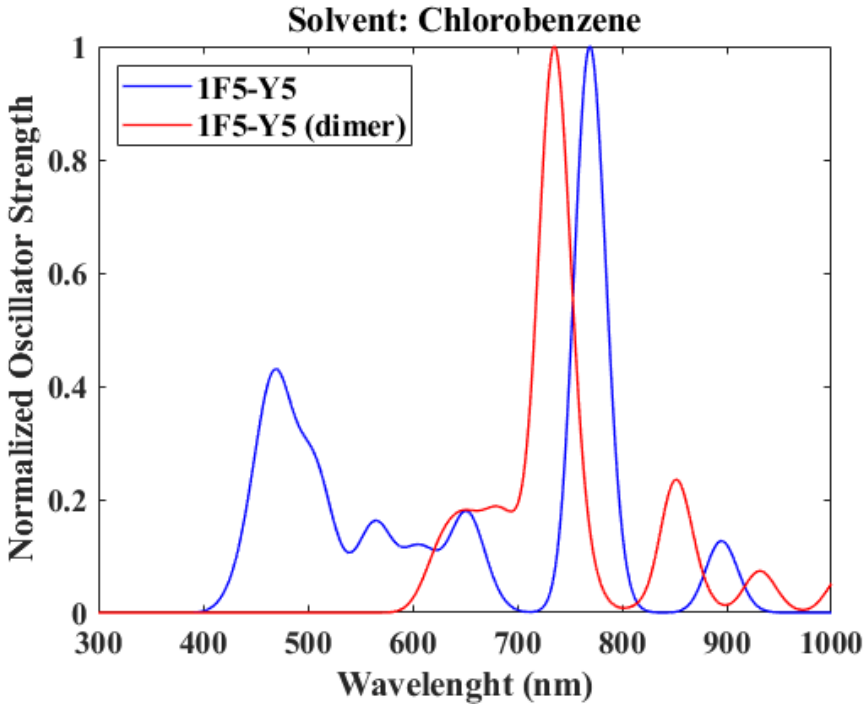

Figure 5.11. Normalized absorption spectra of PF5-Y5 (1F5-Y5) and its dimer in chlorobenzene solution, constructed from 50 vertical transitions dressed in Gaussian line shapes (half-bandwidth = 30 nm). The functional TPSSh was used for all curves.

5.3 Optical gap and exciton binding energies

The optical gap for both Y5 and PF5-Y5 (both as lone molecules and in dimer-formation), calculated as the energy of the first optically allowed electronic transition, can be found in Table 5.2. Note that this transition does not always align with the main peak in the absorption spectrum, e.g., see Figure 5.7, Figure 5.9 or Figure 5.10.

Table 5.2. Optical gap energies (E_{opt}) for Y5 and PF5-Y5 and their respective dimers. *Experimental data is obtained from a full OPV device and is taken from [2]. **Estimated from the position of the main peak in the experimentally obtained spectra (in chlorobenzene), see Figure 5.8.

Molecule	**Functional**	$\boldsymbol{E_{opt}}$ (eV)
Y5	Experimental	1.44*
PF5-Y5	Experimental	1.50*
Y5	Experimental	1.70**
PF5-Y5	Experimental	1.65**
Y5	M06-D3	1.83
Y5	TPSSh	1.64
1F5-Y5	M06-D3	1.77
1F5-Y5	TPSSh	1.38
2F5-Y5	M06-D3	1.76
2F5-Y5	TPSSh	1.35
Y5 (dimer)	M06-D3	1.55
Y5 (dimer)	TPSSh	1.30
1F5-Y5 (dimer)	M06-D3	1.48
1F5-Y5 (dimer)	TPSSh	1.09

From Table 5.2 we can see that optical gap (E_{opt}) obtained using M06-D3 are consistently higher than those obtained using TPSSh. This is in-line with obtained absorption spectra, where M06-D3 consistently return spectra that appear blueshifted compared to those of TPSSh. Furthermore, we can see that as the oligomer length increases, the optical gap decreases ($0.01\ eV$ for M06-D3 and $0.03\ eV$ for TPSSh, i.e., a decrease on the same order as what was observed for the fundamental gap).

The computed optical gaps of Y5 and PF5-Y5 (non-dimer) align poorly with experimentally obtained values (marked with *), both for M06-D3 and TPSSh. It

should however be noted that those values were experimentally determined on a complete OPV device (active layer: PBDP-T:Y5 and PBDB-T:PF5-Y5 respectively), and as such should not exactly reflect the optical gap of either Y5 or PF5-Y5, but rather a combination of both donor and acceptor material and their morphology in the active layer. The active layer of the complete device also had a neat film structure, as such, aggregation effects could play a vital role; and obtained values for the Y5 and PF5-Y5 dimers align much better with experimental values, particularly those obtained using M06-D3 ($\Delta E_{opt} = 0.11\ eV$ for Y5 and $\Delta E_{opt} = 0.02\ eV$ for PF5-Y5).

Estimating the optical gap from the main peak of the experimentally obtained spectra more closely resembles the method used to computationally determine the optical gap; and optical gaps estimated in this way (marked with **) align closer to computationally obtained values for the non-dimers than that of their respective dimers (e.g., $\Delta E_{opt} =$ 0.06 eV for Y5 and 0.4 eV for Y5 (dimer), both obtained using TPSSh).

Calculated exciton binding energies ($E_b = E_g - E_{opt}$) and the effects of relaxation, as well as thermal contributions, can be found in Table 5.3.

Table 5.3. Optical, fundamental (full, adiabatic, and vertical approach) gap energies (data from Table 5.1 and Table 5.2), as well as the respective exciton binding energy, for Y5 and PF5-Y5. *Experimental data is obtained from a full OPV device and is taken from [2]. **Estimated from the position of the main peak in the experimentally obtained spectra (in chlorobenzene), see Figure 5.8.

Molecule	**Functional**	E_{opt} (eV)	$E_{g_{full}}$ (eV)	$E_{g_{adia}}$ (eV)	$E_{g_{vert}}$ (eV)	$E_{b_{full}}$ (eV)	$E_{b_{adia}}$ (eV)	$E_{b_{vert}}$ (eV)
Y5	Experimental	1.44*	1.67			0.23		
PF5-Y5	Experimental	1.50*	1.68			0.18		
Y5	Experimental	1.70**	1.67			-0.03		
PF5-Y5	Experimental	1.65**	1.68			0.03		
Y5	M06-D3	1.83	1.79	1.95	2.12	-0.04	0.12	0.29
Y5	TPSSh	1.64	1.67	1.77	1.95	0.03	0.13	0.31
1F5-Y5	M06-D3	1.77	1.61	1.89	2.13	-0.16	0.12	0.36
1F5-Y5	TPSSh	1.38	1.19	1.53	1.73	-0.19	0.15	0.35
2F5-Y5	M06-D3	1.76		2.09	2.10		0.33	0.34
2F5-Y5	TPSSh	1.35						

From the data in Table 5.3 we can see that in general, even though there is a significant difference between both fundamental and optical gaps obtained using M06-D3 and TPSSh, the resulting exciton binding energies are very comparable between the two functionals. This holds true for all cases (full, adiabatic, and vertical) and for both Y5 and PF5-Y5, with one exception, the exciton binding energy for 2F5-Y5 calculated using M06-D3 and the adiabatic approach.

Furthermore, we can see that both thermal contributions and relaxation clearly acts to decrease the exciton binding energy for both Y5 and PF5-Y5. Accounting for neither relaxation nor thermal effects ($E_{b_{vert}}$) have resulting exciton binding energies for Y5 around $E_b = 0.30\ eV$ and $E_b = 0.35\ eV$ for PF5-Y5.

Relaxation ($E_{b_{adia}}$) reduces the exciton binding energy by roughly $0.15 - 0.20\ eV$ for both Y5 and PF5-Y5, except for the same outlier mentioned above (2F5-Y5 (M06-D3)) that instead saw a reduction of only $0.01\ eV$.

Thermal contributions affect PF5-Y5 significantly more than Y5, reducing the exciton binding energy another $0.16\ eV$ for Y5 and $\sim 0.3\ eV$ for PF5-Y5. Taking all effects into account ($E_{b_{fund}}$) results in very small exciton binding energies for Y5 (even slightly negative for M06-D3). PF5-Y5 (particularly 1F5-Y5 calculated using TPSSh) reaches a considerable negative exciton binding energy of $-0.19\ eV$, which would mean that once the system is given enough time to relax and thermal (vibrational) effects to take place, the polarization effects from the surrounding (in this case the solvent) becomes stronger than the Coulomb attraction of the excitons. Negative exciton binding energies would be beneficial in the pursuit of minimizing risk for exciton recombination, and have previously been realized in solid state devices with strong aggregation effects [49].

6 Conclusion

This thesis has investigated the promising non-fullerene polymer acceptor PF5-Y5 and to an extent also one of its build blocks, the small molecule acceptor Y5, using DFT and TD-DFT.

The choice of functional (i.e., the description of the exchange-correlation interaction) is shown to have significant impact on the obtained redox potentials and fundamental gap. As only two functionals have been used in this work, no general remarks can be made, only specifics of the two functionals (M06-D3 and TPSSh).

Redox potentials (and therefore also the fundamental gap) calculated using M06-D3 align quite well with experimental values. TPSSh overestimates both the reduction and oxidation energy. The oxidation energy in the case of PF5-Y5 was significantly overestimated, and the resulting fundamental gap was $0.49\ eV$ below experimentally obtained values.

Absorption spectra calculated using different functionals have similar general features but are shifted from one another (TPSSh spectra align better with experimentally obtained spectra and are redshifted across all wavelengths compared to spectra obtained using M06-D3). As the optical gap is tied to the electronic transitions making up the absorption spectrum, this also means that optical gaps obtained using M06-D3 are larger than those obtained using TPSSh.

While both the fundamental and optical gaps are significantly affected by the choice of functional; it does not appear to significantly affect obtained exciton binding energies as the effects to the fundamental and optical gaps cancel each other out.

The oligomer length was shown to slightly reduce both the fundamental and optical gaps ($\sim 0.1 - 0.3\ eV$ for each repeated monomer). As such, the effects on the exciton binding energy should at most be quite small, as reducing both gaps by an equal amount will cause their contributions to cancel each other out. Longer oligomers may however increase the risk of aggregation in real devices, which has been shown to have a significant effect on the optical gap.

Relaxation and thermal contributions to Gibbs free energy turned out to have the most impact of the parameters tested. Both relaxation and thermal contributions work to raise the oxidation energy and decrease the reduction energy, resulting in significantly lowering the fundamental gap ($\sim 0.4 - 0.5\, eV$); in turn also lowering the exciton binding energy by a similar amount.

Although not part of the initial aim, this work has also shown that combining first principal calculations with empirical corrections (in this case linear regression towards a dataset) not only is a good predictor of material properties, but also a computationally cost-efficient method.

7 Outlook

As this thesis revolved around an atomic model of PF5-Y5, a logical next step would be to investigate the molecular dynamics of the system as well, bringing even more light on important thermodynamic properties.

The choice of functional has been shown to have a significant impact on the resulting data. A survey testing a large amount of different functionals to find those that best reproduces values from experiments, not only on PF5-Y5 but on a group of organic acceptor materials, could therefore be an interesting future study. Furthermore, a less computationally heavy combination of functional and basis set than the ones used in this thesis could be used. This would allow vibrational frequency calculations on longer oligomers and would allow better characterizing of the effects due to oligomer length.

8 Bibliography

[1] A. Karki, A. J. Gillett, R. H. Friend, and T.-Q. Nguyen, 'The Path to 20% Power Conversion Efficiencies in Nonfullerene Acceptor Organic Solar Cells', *Adv. Energy Mater.*, vol. 11, no. 15, p. 2003441, 2021, doi: 10.1002/aenm.202003441.

[2] Q. Fan *et al.*, 'Over 14% efficiency all-polymer solar cells enabled by a low bandgap polymer acceptor with low energy loss and efficient charge separation', *Energy Environ. Sci.*, vol. 13, no. 12, pp. 5017–5027, Dec. 2020, doi: 10.1039/D0EE01828G.

[3] G. Zhang *et al.*, 'Delocalization of exciton and electron wavefunction in non-fullerene acceptor molecules enables efficient organic solar cells', *Nat. Commun.*, vol. 11, no. 1, p. 3943, Aug. 2020, doi: 10.1038/s41467-020-17867-1.

[4] L. Benatto, C. F. N. Marchiori, C. M. Araujo, and M. Koehler, 'Molecular origin of efficient hole transfer from non-fullerene acceptors: insights from first-principles calculations', *J. Mater. Chem. C*, vol. 7, no. 39, pp. 12180–12193, Oct. 2019, doi: 10.1039/C9TC03563J.

[5] A. Armin *et al.*, 'A History and Perspective of Non-Fullerene Electron Acceptors for Organic Solar Cells', *Adv. Energy Mater.*, vol. 11, no. 15, p. 2003570, 2021, doi: 10.1002/aenm.202003570.

[6] Y. Zhang, I. D. W. Samuel, T. Wang, and D. G. Lidzey, 'Current Status of Outdoor Lifetime Testing of Organic Photovoltaics', *Adv. Sci.*, vol. 5, no. 8, p. 1800434, 2018, doi: 10.1002/advs.201800434.

[7] 'Best Research-Cell Efficiency Chart'. https://www.nrel.gov/pv/cell-efficiency.html (accessed Dec. 18, 2021).

[8] J.-L. Bredas, 'Mind the gap!', *Mater. Horiz.*, vol. 1, no. 1, pp. 17–19, Nov. 2013, doi: 10.1039/C3MH00098B.

[9] '7.4: Electronic Spectroscopy', *Chemistry LibreTexts*, Oct. 28, 2014. https://chem.libretexts.org/Courses/University_of_California_Davis/UCD_Chem_107B%3A_Physical_Chemistry_for_Life_Scientists/Chapters/7%3A_Spectroscopy/7.4%3A_Electronic_Spectroscopy (accessed Dec. 22, 2021).

[10] A. Banerji, M. W. Tausch, and U. Scherf, 'Classroom Experiments and Teaching Materials on OLEDs with Semiconducting Polymers', *Educ. Quím.*, vol. 24, no. 1, pp. 17–22, Jan. 2013, doi: 10.1016/S0187-893X(13)73190-2.

[11] 'Electronic Spectra of Molecules'. http://hyperphysics.phy-astr.gsu.edu/hbase/molecule/molelect.html (accessed Dec. 22, 2021).

[12] B. H. Bransden and C. Joachain, *Quantum Mechanics (Second Edition)*. 2000.

[13] O. Morawski, J. Karpiuk, P. Gawryś, and A. L. Sobolewski, 'Aggregation controlled photoluminescence of hexaazatri-naphthylene (HATN) – an experimental and theoretical study', *Phys. Chem. Chem. Phys.*, vol. 22, no. 27, pp. 15437–15447, 2020, doi: 10.1039/D0CP01289K.

[14] 'Benzene', *Wikipedia*. Dec. 05, 2021. Accessed: Dec. 19, 2021. [Online]. Available: https://en.wikipedia.org/w/index.php?title=Benzene&oldid=1058805141

[15] S. R. Forrest, 'Excitons and the lifetime of organic semiconductor devices', *Philos. Transact. A Math. Phys. Eng. Sci.*, vol. 373, no. 2044, p. 20140320, Jun. 2015, doi: 10.1098/rsta.2014.0320.

[16] C. Deibel and V. Dyakonov, 'Polymer-Fullerene Bulk Heterojunction Solar Cells', *Rep. Prog. Phys.*, vol. 73, Mar. 2010, doi: 10.1088/0034-4885/73/9/096401.
[17] T. Linderl *et al.*, 'Energy Losses in Small-Molecule Organic Photovoltaics', *Adv. Energy Mater.*, vol. 7, no. 16, p. 1700237, 2017, doi: 10.1002/aenm.201700237.
[18] C. W. Tang, 'Two-layer organic photovoltaic cell', *Appl. Phys. Lett.*, vol. 48, no. 2, pp. 183–185, Jan. 1986, doi: 10.1063/1.96937.
[19] 'Polymer Photovoltaic Cells: Enhanced Efficiencies via a Network of Internal Donor-Acceptor Heterojunctions'. https://www.science.org/doi/10.1126/science.270.5243.1789 (accessed Dec. 19, 2021).
[20] D. S. J. Clark, 'The Quantum Many-Body Problem', May 04, 2003. http://cmt.dur.ac.uk/sjc/thesis_ppr/node5.html (accessed Dec. 13, 2021).
[21] J. Thijssen, *Computational Physics*, 2nd ed. Cambridge: Cambridge University Press, 2007. doi: 10.1017/CBO9781139171397.
[22] M. Born and J. R. Oppenheimer, 'On the Quantum Theory of Molecules', 1927, Accessed: Dec. 13, 2021. [Online]. Available: https://elib.bsu.by/handle/123456789/154381
[23] V. Fock, 'Näherungsmethode zur Lösung des quantenmechanischen Mehrkörperproblems', *Z. Für Phys.*, vol. 61, no. 1, pp. 126–148, Jan. 1930, doi: 10.1007/BF01340294.
[24] J. C. Slater, 'A Simplification of the Hartree-Fock Method', *Phys. Rev.*, vol. 81, no. 3, pp. 385–390, Feb. 1951, doi: 10.1103/PhysRev.81.385.
[25] E. Kaxiras and J. D. Joannopoulos, 'Quantum Theory of Materials', *Higher Education from Cambridge University Press*, Apr. 18, 2019. https://www.cambridge.org/highereducation/books/quantum-theory-of-materials/755973CFD3AA7CF69B3C2380D3F5D16D (accessed Dec. 13, 2021).
[26] P. Hohenberg and W. Kohn, 'Inhomogeneous Electron Gas', *Phys. Rev.*, vol. 136, no. 3B, pp. B864–B871, Nov. 1964, doi: 10.1103/PhysRev.136.B864.
[27] W. Kohn and L. J. Sham, 'Self-Consistent Equations Including Exchange and Correlation Effects', *Phys. Rev.*, vol. 140, no. 4A, pp. A1133–A1138, Nov. 1965, doi: 10.1103/PhysRev.140.A1133.
[28] 'The Nobel Prize in Chemistry 1998', *NobelPrize.org*. https://www.nobelprize.org/prizes/chemistry/1998/summary/ (accessed Dec. 11, 2021).
[29] E. Fermi, 'Un metodo statistico per la determinazione di alcune prioprietà dell'atomo.', *Rendiconti Acad. Dei Lincei*, vol. 6, pp. 602–607, 1927.
[30] L. H. Thomas, 'The calculation of atomic fields', *Math. Proc. Camb. Philos. Soc.*, vol. 23, no. 5, pp. 542–548, Jan. 1927, doi: 10.1017/S0305004100011683.
[31] J. Sun, J. W. Furness, and Y. Zhang, 'Chapter 4 - Density functional theory', in *Mathematical Physics in Theoretical Chemistry*, S. M. Blinder and J. E. House, Eds. Elsevier, 2019, pp. 119–159. doi: 10.1016/B978-0-12-813651-5.00004-8.
[32] S. Lundqvist and N. H. March, 'Theory of the inhomogeneous electron gas', 1983. doi: 10.1007/978-1-4899-0415-7.

[33] M. Segall, ‘The Application of Total Energy Pseudopotential Calculations to Biological Molecules: First Year Report’. 1995.
[34] J. Tao, J. P. Perdew, V. N. Staroverov, and G. E. Scuseria, ‘Climbing the Density Functional Ladder: Nonempirical Meta--Generalized Gradient Approximation Designed for Molecules and Solids’, *Phys. Rev. Lett.*, vol. 91, no. 14, p. 146401, Sep. 2003, doi: 10.1103/PhysRevLett.91.146401.
[35] S. Sousa, P. Fernandes, and M. Ramos, ‘General Performance of Density Functionals’, *J. Phys. Chem. A*, vol. 111, pp. 10439–52, Nov. 2007, doi: 10.1021/jp0734474.
[36] Y. Zhao and D. G. Truhlar, ‘The M06 suite of density functionals for main group thermochemistry, thermochemical kinetics, noncovalent interactions, excited states, and transition elements: two new functionals and systematic testing of four M06-class functionals and 12 other functionals’, *Theor. Chem. Acc.*, vol. 120, no. 1, pp. 215–241, May 2008, doi: 10.1007/s00214-007-0310-x.
[37] S. Grimme, J. Antony, S. Ehrlich, and H. Krieg, ‘A consistent and accurate ab initio parametrization of density functional dispersion correction (DFT-D) for the 94 elements H-Pu’, *J. Chem. Phys.*, vol. 132, no. 15, p. 154104, Apr. 2010, doi: 10.1063/1.3382344.
[38] L. Goerigk and S. Grimme, ‘A thorough benchmark of density functional methods for general main group thermochemistry, kinetics, and noncovalent interactions’, *Phys. Chem. Chem. Phys.*, vol. 13, no. 14, pp. 6670–6688, Apr. 2011, doi: 10.1039/C0CP02984J.
[39] K. P. Jensen, ‘Bioinorganic Chemistry Modeled with the TPSSh Density Functional’, *Inorg. Chem.*, vol. 47, no. 22, pp. 10357–10365, Nov. 2008, doi: 10.1021/ic800841t.
[40] E. Runge and E. K. U. Gross, ‘Density-Functional Theory for Time-Dependent Systems’, *Phys. Rev. Lett.*, vol. 52, no. 12, pp. 997–1000, Mar. 1984, doi: 10.1103/PhysRevLett.52.997.
[41] F. Jensen, *Introduction to Computational Chemistry*. John Wiley & Sons, 2017.
[42] ‘Tetralith’. https://www.nsc.liu.se/systems/tetralith/ (accessed Dec. 13, 2021).
[43] A. D. Bochevarov *et al.*, ‘Jaguar: A high-performance quantum chemistry software program with strengths in life and materials sciences’, *Int. J. Quantum Chem.*, vol. 113, no. 18, pp. 2110–2142, 2013, doi: 10.1002/qua.24481.
[44] Y. Takano and K. N. Houk, ‘Benchmarking the Conductor-like Polarizable Continuum Model (CPCM) for Aqueous Solvation Free Energies of Neutral and Ionic Organic Molecules’, *J. Chem. Theory Comput.*, vol. 1, no. 1, pp. 70–77, Jan. 2005, doi: 10.1021/ct049977a.
[45] D. Young, ‘Spin Contamination’. http://www.ccl.net/cca/documents/dyoung/topics-orig/spin_cont.html (accessed Dec. 17, 2021).
[46] R. Barros Neves de Araujo *et al.*, ‘Designing strategies to tune reduction potential of organic molecules for sustainable high capacity battery application’, *J. Mater. Chem. A*, vol. 5, Jan. 2017, doi: 10.1039/C6TA09760J.
[47] ‘Optoelectronics Properties’. https://www.schrodinger.com//sites/default/files/s3/mkt/Documentation/2020-

4/docs/Documentation.htm#materials_help/optoelectronics_properties.html?Highlight=Optoelectronics%20Properties (accessed Dec. 16, 2021).

[48] R. E. Easton, D. J. Giesen, A. Welch, C. J. Cramer, and D. G. Truhlar, 'The MIDI! basis set for quantum mechanical calculations of molecular geometries and partial charges', *Theor. Chim. Acta*, vol. 93, no. 5, pp. 281–301, May 1996, doi: 10.1007/BF01127507.

[49] L. Zhu, J. Zhang, Y. Guo, C. Yang, Y. Yi, and Z. Wei, 'Small Exciton Binding Energies Enabling Direct Charge Photogeneration Towards Low-Driving-Force Organic Solar Cells', *Angew. Chem. Int. Ed.*, vol. 60, no. 28, pp. 15348–15353, 2021, doi: 10.1002/anie.202105156.